The Astrophysical Journal Supplement Series, 263:13 (21pp), 2022 November https://doi.org/10.3847/1538-4365/ac9127

A *Q*-band Line Survey toward Orion KL Using the Tianma Radio Telescope

Xunchuan Liu (刘训川)[1], Tie Liu[1], Zhiqiang Shen[1], Sheng-Li Qin[2], Qiuyi Luo[1,3], Yu Cheng[1,4], Qilao Gu[1], Tianwei Zhang[5], Feng-Yao Zhu[6], Sheng-Yuan Liu[7], Xing Lu[1], Rongbing Zhao[1], Weiye Zhong[1], Yajun Wu[1], Juan Li[1], Zhang Zhao[1], Jinqing Wang[1], Qinghui Liu[1], Bo Xia[1], Bin Li[1], Li Fu[1], Zhen Yan[1], Chao Zhang[1], Lingling Wang[1], Qian Ye[1], Ken'ichi Tatematsu[8], Hongli Liu[2], Hsien Shang[7], Fengwei Xu[9], Chin-Fei Lee[7], Chao Zhang[10], and Somnath Dutta[7]

[1] Shanghai Astronomical Observatory, Chinese Academy of Sciences, Shanghai 200030, People's Republic of China; liuxunchuan@shao.ac.cn, zshen@shao.ac.cn, liutie@shao.ac.cn
[2] Department of Astronomy, Yunnan University, Kunming, 650091, People's Republic of China
[3] School of Astronomy and Space Sciences, University of Chinese Academy of Sciences, No. 19A Yuquan Road, Beijing 100049, People's Republic of China
[4] National Astronomical Observatory of Japan, 2-21-1 Osawa, Mitaka, Tokyo, 181-8588, Japan
[5] I. Physikalisches Institut, Universität zu Köln, Zülpicher Straße 77, D-50937 Köln, Germany
[6] Center for Intelligent Computing Platforms, Zhejiang Laboratory, Hangzhou, 311100, People's Republic of China
[7] Institute of Astronomy and Astrophysics, Academia Sinica, Roosevelt Road, Taipei 10617, Taiwan (R.O.C.)
[8] Nobeyama Radio Observatory, National Astronomical Observatory of Japan, National Institutes of Natural Sciences, 462-2 Nobeyama, Minamimaki, Minamisaku, Nagano 384-1305, Japan
[9] Kavli Institute for Astronomy and Astrophysics, Peking University, 5 Yiheyuan Road, Haidian District, Beijing 100871, People's Republic of China
[10] Institute of Astronomy and Astrophysics, School of Mathematics and Physics, Anqing Normal University, Anqing, People's Republic of China
Received 2022 July 15; revised 2022 September 5; accepted 2022 September 7; published 2022 November 9

Abstract

We have conducted a line survey toward Orion KL using the *Q*-band receiver of the Tianma 65 m radio telescope (TMRT), covering 34.8–50 GHz with a velocity resolution between 0.79 and 0.55 km s^{-1}, respectively. The observations reach a sensitivity of the level of 1–8 mK, proving that the TMRT is sensitive for conducting deep-line surveys. In total, 597 Gaussian features are extracted. Among them, 177 radio recombination lines (RRLs) are identified, including 126, 40, and 11 RRLs of hydrogen, helium, and carbon, with a maximum Δn of 16, 7, and 3, respectively. The carbon RRLs are confirmed to originate from photodissociation regions with a $V_{\rm LSR} \sim 9$ km s^{-1}. In addition, 371 molecular transitions of 53 molecular species are identified. Twenty-one molecular species of this survey were not firmly detected in the *Q* band by Rizzo et al., including species such as H_2CS, HCOOH, C_2H_5OH, $H_2^{13}CO$, H_2CCO, CH_3CHO, CH_2OCH_2, HCN $\upsilon_2 = 1$, and CH_3OCHO $\upsilon_t = 1$. In particular, the vibrationally excited states of ethyl cyanide (C_2H_5CN $\upsilon 13/\upsilon 21$) are for the first time firmly detected in the *Q* band. NH_3 (15,15) and (16,16) are identified, and they are so far the highest transitions of the NH_3 inversion lines detected toward Orion KL. All of the identified lines can be reproduced by a radiative transfer model.

Unified Astronomy Thesaurus concepts: Molecular clouds (1072); Molecular spectroscopy (2095); H II regions (694); Star forming regions (1565)

Supporting material: data behind figure, figure set, machine-readable tables

1. Introduction

The spectral line survey is one of the best ways to study the physical and astrochemical properties of astronomical objects. An unbiased wide-band line survey is generally time-consuming, and thus usually focuses toward the most representative objects of its kind, such as the Orion KL, IRC +10216, W51, TMC-1, and Sgr B2 (e.g., Johansson et al. 1984; Bell et al. 1993; Kaifu et al. 2004; Belloche et al. 2013; Zhang et al. 2017; McGuire et al. 2020; Cernicharo et al. 2021; Pardo et al. 2022; Tercero et al. 2021). Among those well-studied objects, the Orion KL is probably the most classical one. It is the closest high-mass star formation region from us (∼414 pc; Menten et al. 2007) with particularly rich chemical and dynamic properties (e.g., Esplugues et al. 2014). The Orion KL has been targeted by tens of line surveys over the past few decades, especially in the millimeter and submillimeter bands with frequency $\nu > 70$ GHz (e.g., Johansson et al. 1984; Turner 1989; Schilke et al. 1997, 2001; White et al. 2003; Comito et al. 2005; Tercero et al. 2010; Esplugues et al. 2013b). In the millimeter and submillimeter bands, the spectrum of Orion KL is crowded with numerous molecular lines.

Emission of the rotational transitions of heavy species is expected in lower-frequency bands thanks to their small rotational constants. Those low-frequency lines tend to be optically thinner and not severely blended. Another benefit of lower-frequency bands is that the intensities of radio recombination lines (RRLs) are stronger and thus easier to be detected (Gordon & Sorochenko 2002). However there are only a few line surveys toward Orion KL at lower-frequency bands in contrast to the ample surveys at frequencies above 70 GHz, as mentioned earlier.

Gong et al. (2015) conducted a radio *K*-band (∼1.3 cm) line survey covering the frequency range between 17.9 and 26.2 GHz using the Effelsberg 100 m telescope. The *K*-band spectrum of Orion KL was found to be dominated by RRLs, which contribute 164 emission lines among the 261 detected ones.

Although the line surveys in the *Q* band (∼40 GHz, 7.5 mm) located between the RRL-dominant centimeter bands and the optically thick molecular line–dominant (sub)millimeter bands could be very helpful in studying the RRLs and emission lines of complex organic molecules (COMs) simultaneously, very few

surveys have been published. Goddi et al. (2009) conducted a line survey (from 42.3–43.6 GHz) using the Green Bank Telescope (GBT) 100 m optimized for the SiO maser emission of Orion KL. Rizzo et al. (2017) conducted a line survey (from 41.5–50 GHz) using the DSS-54 antenna with a diameter of 34 m. They modeled the Q-band spectrum of Orion KL combining their survey and other surveys. The model predicted emission lines of organic molecules such as $H_2^{13}CO$, CH_2OCH_2, and C_2H_5CN $\upsilon 13/\upsilon 21$, but they were not detected or only marginally detected limited by the aperture size, sensitivity, and spectral resolution (∼180 kHz) of the survey of Rizzo et al. (2017). The carbon RRLs are usually blended with helium RRLs, and only several carbon RRLs were spectrally resolved by Rizzo et al. (2017). Thus, a deeper Q-band line survey toward the Orion KL with wider frequency coverage, better sensitivity, and higher spatial and spectral resolution is extremely valuable for complementing surveys at other bands for a comprehensive modeling of the physical and chemical properties of Orion KL.

Employing the Tianma 65 m radio telescope (TMRT) of Shanghai Astronomical Observatory, we conducted a Q-band line survey covering 34.8–50 GHz toward Orion KL. This is the first systematic line survey of the TMRT. This survey reaches a sensitivity on the level of 1–8 mK with a frequency resolution of ∼90 kHz. In this work, we present preliminary results of the TMRT Q-band survey toward Orion KL. The paper is structured as follows: In Section 2 we briefly introduce the equipment and observations setup adopted by this survey, as well as the data reduction process. In Section 3 we describe the procedure for the identification of lines. In Section 4 a simple radiative transfer model is fitted to reproduce the observed Q-band emission lines of Orion KL, including both RRLs and molecular lines. In Section 5, we discuss RRLs and some individual species detected in this survey. Section 6 provides a summary.

2. Observation and Data Reduction

2.1. TMRT

The observations were carried out using the TMRT of the Shanghai Astronomical Observatory.[11] The TMRT is a 65 m diameter fully steerable radio telescope located in a western suburb of Shanghai, China. Receivers from the L to Q band are available, covering a frequency range of 1–50 GHz. The Q-band receiver provides the highest-frequency coverage of TMRT. Before this survey, the Q-band receiver of TMRT was not fully used for single-dish scientific observations, compared to the receivers of the $C/Ku/K$ bands (Li et al. 2016; Zhang et al. 2017; Wu et al. 2019a, 2019b; Xie et al. 2021; Liu et al. 2022).

The Q-band receiver is a two-beam dual-polarization (LCP and RCP) cryogenic receiver, covering a frequency range of 35–50 GHz (Zhong et al. 2018). The two beams cannot work simultaneously at present for spectral line observation limited by the backend. Only beam 2 was employed during our observations. The receiver noise temperatures are roughly 30–40 K, and the system temperature ranges from 60–150 K depending on the frequency and weather conditions (Zhong et al. 2018). The FWHM of the primary beam is ∼30″ at 40 GHz. Pointing was conducted every two hours. The pointing accuracy is better than 5″.

[11] http://english.shao.cas.cn/sbysys/

For spectral line observations, an FPGA-based spectrometer based upon the design of the Versatile GBT Astronomical Spectrometer (VEGAS) was employed as the digital backend system (Bussa & VEGAS Development Team 2012). Twenty-nine observing modes (Mode 1–29) with different frequency bandwidths and resolutions are available. For our observations, Mode 2 was adopted, which provides a set of independent frequency banks with a bandwidth of 1500 MHz each. Three banks were designed for TMRT but only two of them are available at present. Each frequency bank provides data of both left-hand circular polarization (LCP) and right-hand circular polarization (RCP). For each polarization, a frequency bank has 16,384 channels, corresponding to a frequency resolution of 91.553 kHz (∼0.69 km s^{-1} at 40 GHz).

For calibration, the signal of noise diodes was injected lasting for 1 s within each 2 s period. The temperatures of the noise diodes are ∼18 K and ∼12 K for the LCP and RCP, respectively. The aperture efficiency (η_A) at Q band has a dependence on elevation (el) following (Wang et al. 2017)

$$\eta_A = p_0 + p_1 \mathrm{el} + p_2 \mathrm{el}^2 + p_3 \mathrm{el}^3, \quad (1)$$

where p_0, p_1, p_2, and p_3 are 6.33×10^{-2}, 3.47×10^{-3}, 4.11×10^{-4}, and -5.72×10^{-6}, respectively, and el is in degrees. The efficiency decreases significantly for small and large elevation because of gravity deformation. The telescope has an active surface control utilizing actuators to compensate for gravity deformation in the main reflector during observations (Dong et al. 2018). It makes the Q-band aperture efficiency constant (0.5 ± 0.1) for elevation within 15°–80° (Zhong et al. 2018). Under the typical weather condition of TMRT in winter with an air pressure of 1000 mbar and a water vapor density of 8 g cm^{-3}, the zenith atmospheric opacity ranges from 0.07–0.35 in the Q band (35–50 GHz; Wang et al. 2017). The main beam efficiency is ∼0.60 and depends on the elevation and frequency. Calibration uncertainties are estimated to be within 20%.

2.2. Observation

Our observations toward Orion KL were conducted during 2022 March 9–29. The targeted position is R.A. (J2000) = 05:35:14.55, decl. (J2000) = −05:22:31.0 (Figure 1). Position switching observation mode was adopted, with the off points 0.°5 away (in azimuth direction) from the target, and integrating 2 minutes in each position (on/off). Spectra of failed observations (which are wrongly calibrated with abnormal system temperatures larger than 1000 K) were discarded. For each frequency bank, its frequency coverage in sky frequency scale was fixed. The frequency of the local oscillator (LO) did not change during the observation for each frequency setup. The spectrum of each on-off repeat was corrected from the topocentric frame to the frame of local standard of rest (LSR) during data processing. Banks were shifted in frequency to cover 34.5–50 GHz, but always leaving an overlap of >300 MHz between two adjacent configurations. For each frequency setup, a telescope time of 3–10 hr was consumed, depending on the weather conditions.

2.3. Data Reduction

Combining all scans of observations from all frequency setups, a full-frequency coverage between 34.8 and 50 GHz was achieved. The spectra were then chopped into segments of

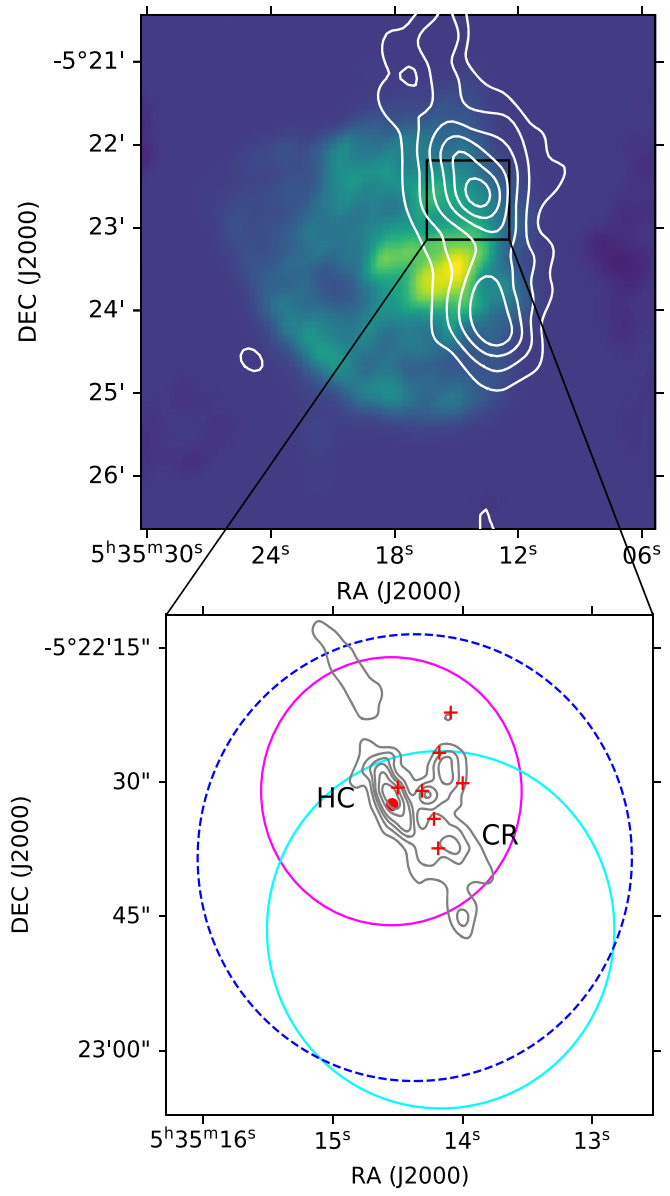

Figure 1. Upper: contours of SCUBA 850 μm dust emission (Di Francesco et al. 2008) overlaid on the 6 cm VLA continuum image. Lower: continuum map of Orion KL at 230 GHz from the ALMA-SV line survey. The hot core region and the compact ridge are indicated by HC and CR, respectively. The red crosses represent the infrared clumps (Shuping et al. 2004). The red dot marks HC(S) (Neill et al. 2013). The purple, cyan, and blue circles represent the beams from this survey, Gong et al. (2015), and Rizzo et al. (2017), respectively. The blue circle is dashed since Rizzo et al. (2017) did not mention their targeting center, and hence, only the size of the blue circle is meaningful.

100 MHz in bandwidth, and Gildas/CLASS[12] was adopted to fit and subtract the spectral baselines for each segment. We combined all of the segments weighted by their noise levels to obtain a Q-band spectrum of Orion KL. We further converted the frequency of the spectrum from the frame of LSR to the rest frame of Orion KL assuming a systematic velocity of Orion KL ($V_{\rm LSR}$) of 6 km s^{-1}, through

$$f_{\rm final} = f_{\rm LSR}\left(1 + \frac{V_{\rm LSR}}{c}\right). \quad (2)$$

[12] https://www.iram.fr/IRAMFR/GILDAS/

Here, c is the light speed, $f_{\rm LSR}$ is the spectral frequency in the frame of LSR, and $f_{\rm final}$ is the frequency of the final spectrum. The frequencies related to Orion KL are always referred to as $f_{\rm final}$ throughout this work. The final spectrum is shown in Figure 2. The rms noise of the final spectrum (in $T_{\rm MB}$ scale with a frequency resolution of 91 kHz) ranges from 1.8–8 mK, with a mean value of 4.2 mK and a standard deviation of 1.2 mK (Figure 3).

The example zoomed-in spectra chopped into subbands of 250 MHz are displayed in Figure 4. The complete figure set (61 images) is available. Figure 5 shows a fraction of the final spectrum from this survey and from Rizzo et al. (2017) for comparison.

3. Line Identification

3.1. Extract Possible Emission Features

The spectrum was visually checked for a preliminary identification of bad channels and channels containing possible line features. The bad channels were masked out. Gaussian fittings were then applied to the possible line features one by one. For strong lines with obvious non-Gaussian shapes or multiple blended emission components, multiple Gaussian fittings were applied to approach their line profiles. In total, 597 Gaussian components were extracted as listed in Tables 3 and 4 in the Appendix. Table 3 lists the molecular lines, and Table 4 lists the RRLs that are not blended with molecular lines.

3.2. Identification of RRLs

The RRLs of hydrogen (H) and helium (He) are from the H II regions, with typical line widths >10 km s^{-1} (Gordon & Sorochenko 2002). The emission features with line widths larger than 10 km s^{-1} were first labeled as candidates of RRLs of H and He. Since the RRLs of carbon (C) mainly originate from the photodissociation regions (PDRs) between the M42 and the Orion Bar (e.g., Cuadrado et al. 2015; Rizzo et al. 2017), the constraint of the line width was not applied to identifying RRLs of carbon. Emission features close to helium RRLs were marked as carbon RRL candidates. We then crossmatched those RRL candidates with the rest frequencies of RRLs of H, He, and C, which can be calculated through

$$\nu_{\rm rest}^{\rm RRL}(n + \Delta n, n) = \nu_0^{\rm RRL}\left(\frac{1}{n^2} - \frac{1}{(n + \Delta n)^2}\right) \text{ MHz}, \quad (3)$$

with $\nu_0^{\rm RRL}$ adopted as 3.28805129×10^9, 3.28939118×10^9, and 3.28969187×10^9 for H, He, and C, respectively (Gordon & Sorochenko 2002). For an RRL candidate that is not blended with strong lines of molecules (e.g., SiO, SO, HC_3N, CH_3OH, CH_3OCH_3, and C_2H_5CN), it was assigned to a specific RRL transition if only one RRL transition can be found within 20 km s^{-1} of it. If it is blended, multiple Gaussian fitting was carefully reconducted to separate the contributions of blended components. We marked an RRL candidate as an unresolved blended line if it was highly blended and inseparable by Gaussian decomposition.

In total, 177 recombination lines are matched, including 126, 40, and 11 lines corresponding to H, He, and, C, respectively. Among them, 39 are blended lines that cannot be well resolved and the other 138 can be spectrally resolved. Basic parameters of the matched RRL lines, including the observed frequency

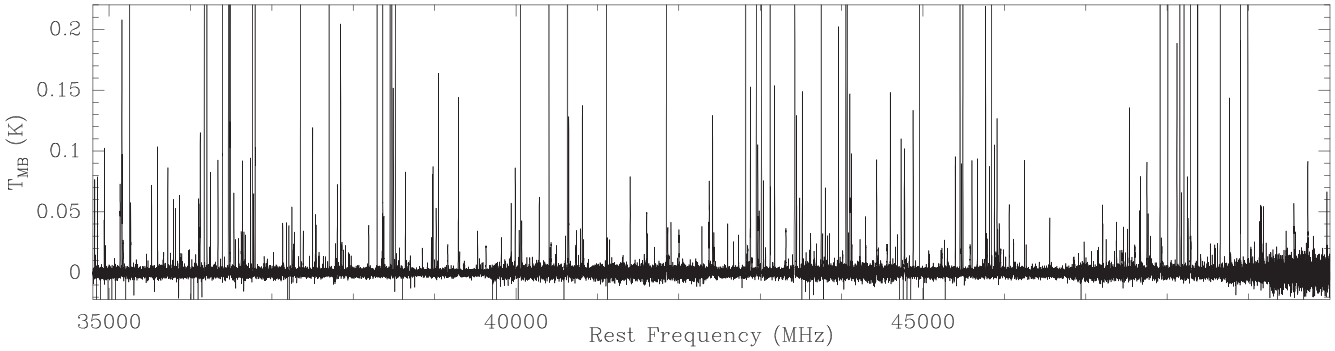

Figure 2. The overview of the Orion KL spectrum in the *Q* band observed by the TMRT.
(The data used to create this figure are available.)

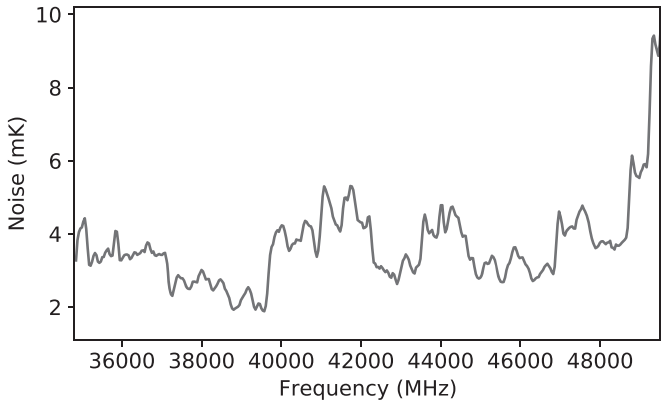

Figure 3. The rms noise of the spectrum. The line features and bad channels (Section 3.1) have been masked out before calculating the rms noise.

($f_{\rm obs}$), the name of the RRL transition, the rest frequency ($f_{\rm rest}$), and the Gaussian fitting results (the integrated intensity $\int T_{\rm MB} dV$, the line width ΔV, and the peak intensity $T_{\rm MB}^{\rm peak}$) are listed in Table 3.

3.3. Identification of Molecular Lines

To identify the emission of molecular lines, we consulted the frequencies of molecular transitions from the databases at the CDMS[13] (Müller et al. 2001), the JPL[14] (Pickett et al. 1998), and the Splatalogue.[15] The transition parameters of C_2H_5CN $\upsilon 13/\upsilon 21$ are adopted from Endres et al. (2021).

The identification of molecular lines started with strong emission features. All strong emission features ($T_{\rm MB}^{\rm peak} > 100$ mK) can be easily assigned with no ambiguities. To identify a weak emission feature, we first checked whether there is a probable transition of the already identified species. If so, we assigned it to that matched species. If not, we searched the databases to find candidate species that have transitions near the objective line and empirically have nonnegligible abundances. For a matched candidate species, we queried the databases to get all its transitions with frequencies covered by this survey. If more than one strong transition (with large line strength and reasonable upper-level energy) of a candidate species has a corresponding emission feature in our spectrum, that candidate species was marked as an identified one. We repeated this process until all emission features have been checked. We then modeled the emission of identified species (including both molecular emission and RRLs; see Section 4). If the blended features can be accounted for only partly by the identified species, we tried to assign the unmatched emission features to unidentified species. If there were strong transitions of a species that cannot be well fitted, that species was removed from the set of identified species. We iterated the above procedure of weak line identification until no further adjustment could be made. The remaining unmatched features are labeled as unidentified (U) lines. Basic parameters of the matched molecular lines, including the observed frequency ($f_{\rm obs}$), the name of the species, the rest frequency ($f_{\rm rest}$), the transition labels, the upper-level energy ($E_{\rm up}$), the Einstein coefficients (A_{ij}), and the Gaussian fitting results, are also listed in Table 3.

In total, 371 molecular transitions of 53 species were identified (Table 1). Here, isotopologues and molecules in different vibrational states are treated as different species. The transition parameters of C_2H_5CN $\upsilon 13/\upsilon 21$ are not publicly available, and we will further discuss this species in Section 5.2.4.

3.4. Unidentified Lines

There are 39 emission features that have not been successfully associated with any RRLs and molecular transitions. They are also listed in Table 3 labeled as "U." Most of them are weak emission features or blended with strong lines (Figure 4). Two doublets (42,732/42,735 and 43,482/43,485 MHz) are exceptions. Their strong intensities cannot be assigned to any RRLs and molecular emission. The nearby strong doublet of SiO maser (43,122/43,124 MHz) with peak intensity >50 K may saturate the system and contribute to these fake doublets. However, this reason can be ruled out since the fake doublets appeared only once, with central frequencies of 42,770 MHz and 44,020 MHz for bank A and bank B, respectively. During the observations of another day with a slightly shifted LO frequency (the central frequencies were 42,750 and 44,000 MHz for bank A and bank B, respectively), such fake doublets did not appear. We have also checked the observations with a larger LO frequency offset (the central frequencies were 42,550 MHz and 43,750 MHz for bank A and bank B, respectively), and such fake doublets still did not appear (Figure 6). The relevant observations were conducted in three different days, and they all covered the SiO $J = 1$–0 maser. Thus, we tend to assign the fake doublets to interference lines arising

[13] https://cdms.astro.uni-koeln.de/cdms/portal/
[14] https://spec.jpl.nasa.gov/
[15] https://splatalogue.online/

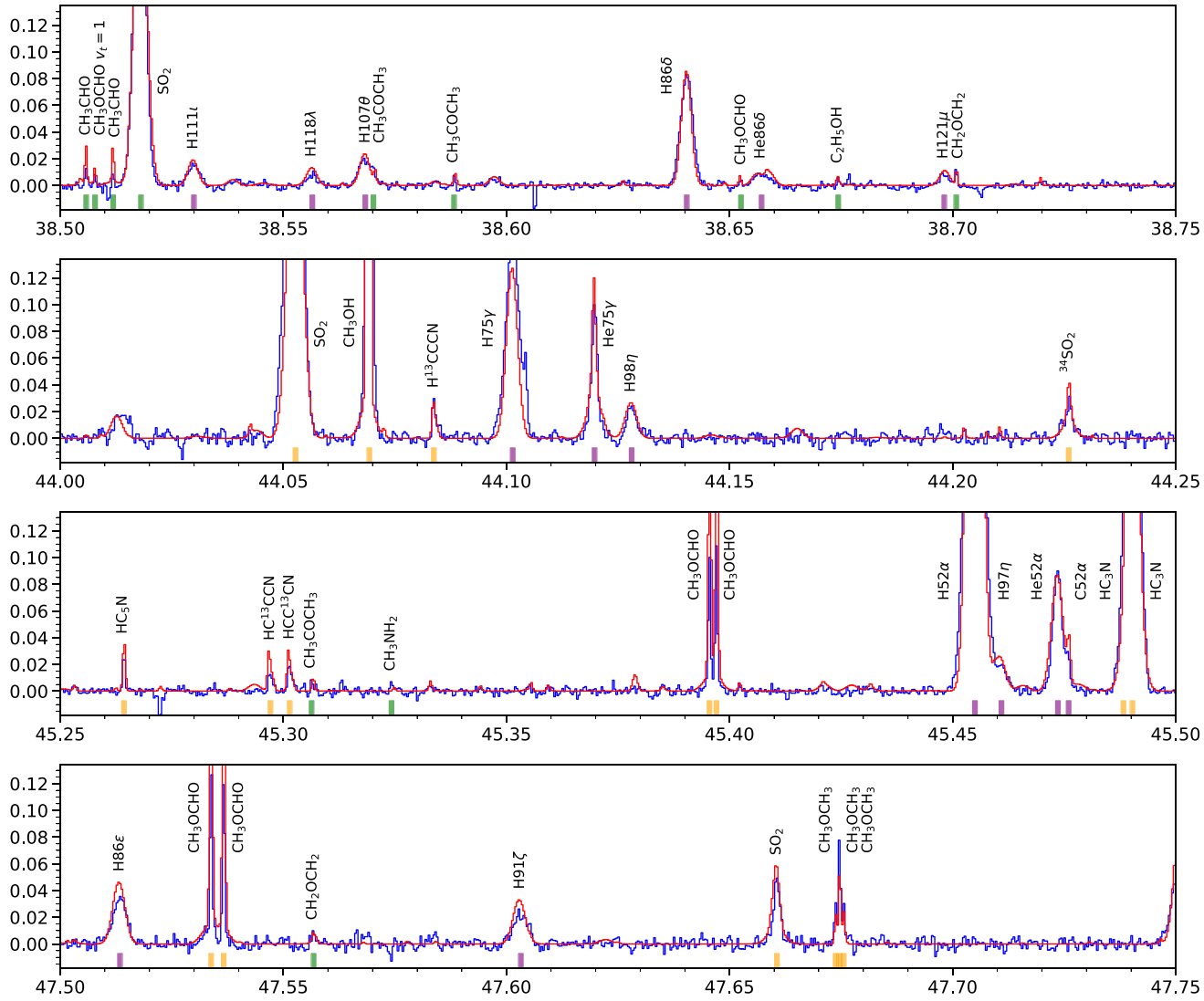

Figure 4. The example zoomed-in spectra of the Orion KL. The complete figure set covering the 34.8–50 GHz is available. The blue line is the Orion KL spectrum observed by the TMRT 65 m, which has been smoothed to have a frequency resolution of 364 kHz (∼2.8 km s^{-1} at 40 GHz). The red line represents the results of model fitting (Section 4). The purple strips denote the detected RRLs. The yellow strips denote the molecular lines, which have also been detected and resolved by Rizzo et al. (2017). The green strips denote the molecular lines detected by TMRT 65 m but have not been detected by Rizzo et al. (2017). The red strips denote the lines of C_2H_5CN $\upsilon 13/\upsilon 21$. The gray strips mark the U lines. The lines of SiO and its isotopologues are not modeled. The x-axis is rest frequency in units of gigahertz (with a Doppler correction applied adopting a V_{LSR} of 6 km s^{-1}). The y-axis is T_{MB} in units of kelvin.

(The complete figure set (61 images) is available.)

from the telescope system under very particular situations. No such phenomena happened during other observation setups.

4. Model Fitting

To reproduce the spectrum of Orion KL observed by the TMRT and reaffirm the line identification, we fit it with a simple radiative transfer model. The emission of Orion KL (especially for strong lines) is complex, with contributions from several physical components including the foreground H II region M42 (Wilson et al. 1997), the PDR between M42 and the molecular cloud (e.g., Natta et al. 1994), the externally heated "compact ridge" (e.g., Mangum & Wootten 1993; Wang et al. 2011; Tahani et al. 2016), the hot cores (e.g., Mangum & Wootten 1993; Jacob et al. 2021), the extended ridge and plateau (e.g., Genzel & Stutzki 1989; Bernal et al. 2021) as well as some other millimeter continuum sources (e.g.,Wu et al. 2014). Since only single-point data were available in our observations, it is difficult to assign the detected emission to specific physical structures within the beam, especially for molecular emission. Most of the detected lines are optically thin even if a beam filling factor of 0.1 is adopted. Thus, the inferred column densities from the model fitting are highly coupled with the source size and the beam filling factor. We note that the spectral modeling of this work is mainly used for line identification, and particular caution should be taken if the modeled parameters (e.g., N_{tot}) listed in Table 2 are used for comparison with results from other authors. The fitted column density of the molecule should be multiplied by a factor accordingly if a different size of the emission region is adopted. The fitted emission measures (EMs) of the H II region and PDR region (Section 4.1.2) are more robust since the emission of RRL is more extended than the observing beam.

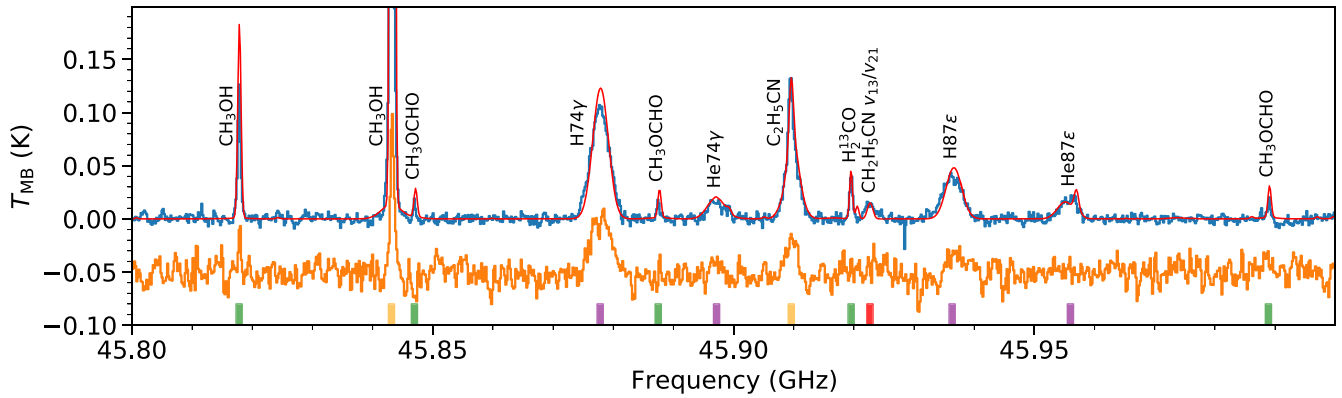

Figure 5. An example of comparison between the spectra of this survey in blue and of Rizzo et al. (2017) in orange. The spectrum shown here has been smoothed to have the same spectral resolution of Rizzo et al. (2017). The red line represents the results of model fitting (Section 4). The bottom purple strips denote the detected RRLs. The yellow strips denote the molecular lines, which have also been firmly detected and resolved by Rizzo et al. (2017). The green strips denote the molecular lines detected by TMRT 65 m but have not been detected by Rizzo et al. (2017). The red strips denote the lines of C_2H_5CN $\upsilon 13/\upsilon 21$. The x-axis is the frequency, which has been converted to the rest frame of Orion KL with a $V_{\rm LSR}$ of 6 km s^{-1} (Section 2.3).

4.1. Model Fitting of RRLs

4.1.1. Emission Model of RRLs

The emission of RRLs was modeled through adding up the spectra of all of the RRL transitions of H, He, and C within the frequency range of this survey. For species X (denoting H and He), its RRL spectrum can be calculated using (Gordon & Sorochenko 2002)

$$\tau_{n_1,n_2} = 3.867 \times 10^{-12} \frac{b_{n_2}}{\Delta\nu} \frac{\Delta n}{n_1} f_{n_1,n_2} \left(1 - \frac{3\Delta n}{2n_1}\right) \frac{\rm EM}{T_e^{5/2}}, \quad (4)$$

and

$$T_{\rm X} = \sum_{n_1,n_2} T_e \tau_{n_1,n_2} \frac{n_X}{n_e} \exp\left(-\frac{\left[\nu - \nu_{\rm rest}^{\rm RRL}(n_1, n_2)(1 - \frac{\upsilon}{c})\right]^2}{2\Delta\nu^2/(8\ln(2))}\right). \quad (5)$$

Here, the parameters are adopted as the values in cgs units, EM is the emission measure, $n_{\rm X}$ is the volume density of X, υ is the velocity, b_{n_2} is the upper-level departure coefficient, and T is the excitation temperature. The optically thin limit ($\tau_{n_1,n_2} \ll 1$) is satisfied for all of the detected RRLs. The term of $\exp(E_{n_2}/kT)$ is omitted in Equation (4) since $E_{n_2} \ll kT$ for the detected RRLs. The oscillator strength f_{n_1,n_2} can be approximated as (Menzel 1968)

$$f_{n_1,n_2} \sim n_1 M_{\Delta n} \left(1 + 1.5\frac{\Delta n}{n_1}\right) \quad (6)$$

for high-level transitions of hydrogen-like atoms. We empirically fitted the values of $M_{\Delta n}$ tabulated in Menzel (1968) as

$$M_{\Delta n} \sim 0.1905(1/\Delta n)^{2.887}. \quad (7)$$

The oscillator strength can be calculated more accurately from the method described in Brocklehurst (1971) and Regemorter & Prudhomme (1979). The accurate values have been used in recent models of Prozesky & Smits (2018) and Zhu et al. (2019, 2022). The modeled spectrum in this work will not change obviously when the more accurate values of f_{n_1,n_2} are adopted.

The electron temperature (T_e) of H II regions are assumed as 8000 K (e.g., Wilson et al. 1997; Zuckerman et al. 1967). If the RRL emitters are in LTE state, the departure coefficients should be unity for all levels. For $n_e = 10^4$ cm^{-3} and $T = 8000$ K, we calculated the population of hydrogen using the method by Zhu et al. (2019, 2022). The departure coefficients b_n increase from 0.85–0.99 as n increases from 50–100. It means that the departure coefficients in Equation (6) cannot be omitted to precisely reproducing the observed RRLs and calculating the EM. The RRLs of H and He from HII regions under strong ultraviolet fields originate from similar emission regions. The states of helium atoms considered in this work are approximately hydrogenic in nature with $n \gg 1$. Storey & Hummer (1995) suggested that the departure coefficients for hydrogen atoms can also be applied to these states of helium atoms.

At large n, the carbon atom is physically similar to H and He; thus, the above equations for H and He are also valid for deriving the emission of carbon RRLs (Salgado et al. 2017). For carbon in PDRs, an electron temperature of 2000 K is adopted considering $(E_{\rm ionize}^{\rm H} - E_{\rm ionize}^{\rm C})/k < 3000$ K. We also try to fit the carbon lines using a T_e of 300 K (Section 4.1.2). We assume that the carbon atoms are in an LTE state with the departure coefficients of carbon adopted as unity, although this is somewhat uncertain.

To determine the values of line widths and velocities of the modeled RRLs, we have referred to the Gaussian fitting results of the detected RRLs (see Table 3 and Section 5.1) and the values of previous studies (Goddi et al. 2009; Gong et al. 2015; Rizzo et al. 2017). The $\Delta\nu$ is the FWHM line width of the modeled spectrum in frequency scale, which can be calculated through

$$\Delta\nu = f_{n_1,n_2}^{\rm RRL} \frac{\Delta\upsilon}{c}. \quad (8)$$

Here, the $\Delta\upsilon$ is fixed as 20 km s^{-1} for H/He RRLs and 5 km s^{-1} for C RRLs. The velocity (in $V_{\rm LSR}$) of H/He and C is fixed as -3 km s^{-1} and 9 km s^{-1}, respectively (see Section 5.1.2 for further discussion).

4.1.2. Fitting Results of RRLs

The beam filling factor of H/He RRLs is adopted as unity, since they mainly originate from the extended M42 HII region.

Table 1
Detected Molecular Species of This Survey[a]

CS	^{34}SO	**HC^{13}CCN**	CH_3CN $v_t = 1$	*NH_2CHO*	$H_2^{13}CO$	**SiO**
^{13}CS	**OCS**	**HCC^{13}CN**	HCN $v_2 = 1$	**CH_3OH**	H_2CCO	**SiO $v = 1$**
^{33}CS	O^{13}CS	HC_3N $v_6 = 1$	**C_2H_3CN**	**$^{13}CH_3OH$**	CH_3CHO	**SiO $v = 2$**
^{34}CS	**OC^{34}S**	**HC_3N $v_7 = 1$**	**C_2H_5CN**	**A-CH_3OH $v_t = 1$**	**CH_3OCHO**	**^{29}SiO**
CCS	**SO_2**	HC_3N $v_7 = 2$	CH_2H_5CN v_{13}/v_{21}	**E-CH_3OH $v_t = 1$**	**CH_3OCHO $v_t = 1$**	**^{30}SiO**
HCS^+	**$^{34}SO_2$**	**HC_5N**	NH_3	C_2H_5OH	CH_2OCH_2	
H_2CS	**HC_3N**	*CH_3NH_2*	**NH_2D**	HCOOH	**CH_3OCH_3**	
SO	**H^{13}CCCN**	CH_3CN	**HNCO**	**H_2CO**	CH_3COCH_3	

Note.
[a] The species in bold have transitions detected and spectrally resolved by Rizzo et al. (2017). Those in italic mean their transitions are marginally detected or highly blended.

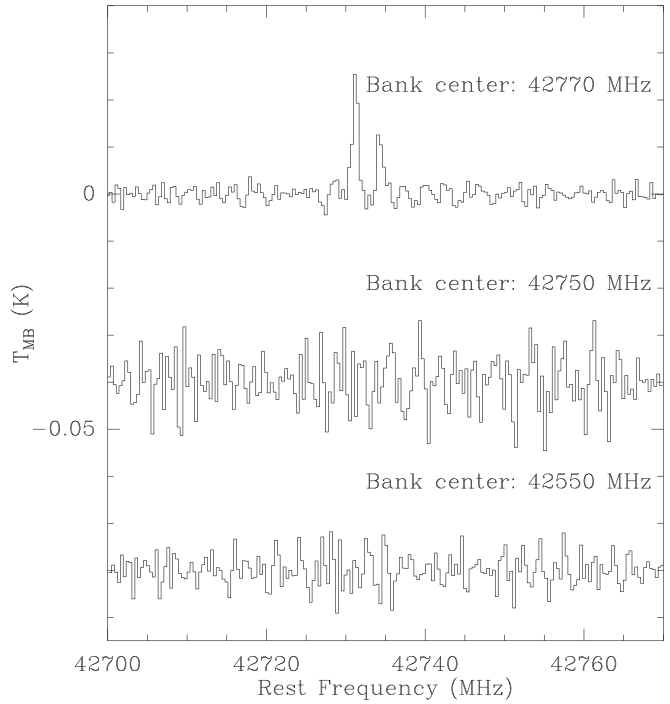

Figure 6. The spectra of the 42,732/42,735 doublet observed in three different days. The fake signals appeared only once under an unknown particular situation, and no such phenomena happened during other observation setups (Section 3.4). The fake doublets are kept in the spectrum shown in Figure 4.

The EM is fitted as 3.9×10^6 cm^{-6} pc. The abundance ratio between He and H (He/H) is fitted to 8.5%. We note that this value is derived with an assumption that the H and He have identical ionized regions. We will further discuss the He/H ratio in Section 5.1.2. The fitted intensities of unblended H/He RRLs are all consistent with the observed values within 20%. The fitted emission measure of HII region (EM^{HII}) is compatible with the value of 7.5×10^6 cm^{-6} pc derived by Dicker et al. (2009) using the 21.5 GHz data of the GBT with a beam size of 33.″5.

The carbon RRLs mainly originate from PDR between the M42 and molecular clouds. Since the main body of the Orion bar is larger than the beam of this survey, a beam filling factor of unity is also adopted for carbon RRLs. If the ionized carbons contribute to most of the electrons within the PDR region, the EM of the PDR can be fitted to $EM^{PDR} = 3.9 \times 10^3$ cm^{-6} pc. If an electron temperature of 300 K (instead of 2000 K) is adopted, the fitting result gives $EM^{PDR} = 1.8 \times 10^2$ cm^{-6} pc.

4.2. Model Fitting of Molecular Lines

4.2.1. Emission Model of Molecular Lines

The molecular emission was modeled by adding up a set of spectral components contributed by different species. A species (denoted as X) may contribute multiple spectral components with different velocities. A spectral component may consist of more than one line feature contributed by different transitions of its corresponding species. Each spectral component is assumed to be in an LTE state with an identical emission source size (D) and the same excitation temperature (T_{ex}) for all transitions of the corresponding species. For each spectral component (denoted as s), its spectrum (T_s in main beam temperature scale) could be modeled through adding up a set of emission lines of the transitions of the corresponding species. Those lines have Gaussian-shaped optical depths with the same line width and T_{ex}. Specifically, a spectral component can be calculated following (e.g., Mangum & Shirley 2015)

$$\tau_{ij}^s = \frac{A_{ij}c^2}{8\pi(\nu_{ij})^2}\left[\exp\left(\frac{h\nu_{ij}}{kT_{ex}}\right) - 1\right]N_{tot}^s\frac{g_u}{Q}\exp\left(\frac{-E_u}{kT_{ex}}\right)\frac{1.06}{\Delta\nu_s} \quad (9)$$

and

$$T_s = \sum_{i,j} f T_{ex}\left\{1 - \exp\left[-\tau_{i,j}^s \exp\left(-\frac{\left[\nu - \nu_{i,j}(1 - \frac{v_s}{c})\right]^2}{2\Delta\nu_s^2/(8\ln(2))}\right)\right]\right\}. \quad (10)$$

Here, τ_{ij}^s is the peak optical depth, N_{tot}^s is the column density of the corresponding species, $\Delta\nu_s$ is the line width in frequency scale ($\Delta\nu = \nu_{i,j}\Delta V_s/c$), f is the beam filling factor $(D/\Theta_{\nu_{i,j}})^2$, $\Theta_{\nu_{i,j}}$ is the beam size at $\nu_{i,j}$, E_u is the upper-level energy, g_u is the degree of degeneracy of the upper level, and Q is the partition function. The Q is a function of T_{ex}, and it could be interpolated from the tabulated values quoted from online databases (Section 3.3). The modeled spectrum of a species is

$$T_X = \sum_s T_s. \quad (11)$$

For each species, we fit T_X to the observed spectrum. Since we only tried to build a radiative transfer model with the goal to reproduce our observed spectrum, source size and T_{ex} for each spectral component are fixed. The values of line widths (ΔV_s), velocity (v_s), and column density (N_{tot}^s) are fitted.

Table 2
Model Parameters

Species[a]	Size[b] (″)	T_{ex} (K)	N_{tot}[c] (cm^{-2})	ΔV (km s^{-1})	V_{lsr} (km s^{-1})	Species	Size (″)	T_{ex} (K)	N_{tot} (cm^{-2})	ΔV (km s^{-1})	V_{lsr} (km s^{-1})
CS	30	100	9.6e+14	15.0	7.0	$^{34}SO_2$	30	50	1.5e+14	4.0	7.0
	10	100	1.2e+16	4.0	8.5		30	200	6.0e+14	10.0	7.0
$C^{34}S$	30	100	6.0e+13	15.0	7.0		30	100	6.0e+14	25.0	7.5
	10	100	8.4e+14	4.0	8.5	HCN $v_2 = 1$	10	200	1.8e+17	4.0	7.0
^{13}CS	30	100	2.4e+13	15.0	7.0	HC_3N	15	100	1.9e+14	3.0	9.0
	10	100	3.0e+14	4.0	8.5		10	100	3.0e+14	7.0	5.5
$C^{33}S$	10	100	6.0e+13	4.0	12.0		10	100	6.0e+14	15.0	5.5
HCS^+	15	100	1.7e+13	2.0	10.0		20	100	1.2e+14	25.0	6.0
H_2CS	15	100	1.1e+15	2.0	8.5	$H^{13}CCCN$	15	100	1.4e+13	4.0	10.0
SO	10	100	1.2e+17	15.0	6.0		10	100	2.4e+13	7.0	5.5
	10	100	2.2e+17	25.0	9.0	$HC^{13}CCN$	15	100	1.4e+13	4.0	10.0
^{34}SO	10	100	4.8e+15	15.0	6.0		10	100	2.4e+13	7.0	5.5
	10	100	9.6e+15	25.0	9.0	$HCC^{13}CN$	15	100	1.4e+13	4.0	10.0
OCS	30	100	1.2e+15	3.0	8.0		10	100	2.4e+13	7.0	5.5
	30	50	7.2e+14	10.0	6.0	HC_3N $v_6 = 1$	10	150	2.4e+15	7.0	5.5
	30	100	7.2e+14	25.0	5.0	HC_3N $v_7 = 1$	10	150	2.4e+15	7.0	5.5
$OC^{34}S$	30	100	6.0e+13	3.0	8.0		10	100	3.6e+15	25.0	6.0
	30	50	3.6e+13	10.0	6.0	HC_3N $v_7 = 2$	10	150	2.4e+15	7.0	5.5
$O^{13}CS$	30	100	2.4e+13	3.0	8.0	HC_5N	10	100	3.6e+13	4.0	8.5
	30	50	2.4e+13	10.0	6.0	CH_3CN	10	200	4.8e+15	6.0	7.0
SO_2	30	50	3.0e+15	4.0	7.0		10	100	6.0e+15	20.0	8.0
	30	200	6.0e+15	10.0	7.0	CH_3CN $v_t = 1$	10	200	4.8e+15	6.0	6.0
	30	100	1.9e+16	25.0	7.5	C_2H_3CN	5	320	3.6e+14	6.0	5.0

Species	Size (″)	T_{ex} (K)	N_{tot} (cm^{-2})	ΔV (km s^{-1})	V_{lsr} (km s^{-1})	Species	Size (″)	T_{ex} (K)	N_{tot} (cm^{-2})	ΔV (km s^{-1})	V_{lsr} (km s^{-1})
	10	100	1.2e+14	6.0	5.0	CH_3CHO	15	50	2.4e+14	3.0	8.0
	5	200	1.1e+14	20.0	3.0		30	150	2.4e+14	25.0	9.0
	10	90	1.6e+14	20.0	3.0	CH_3OCHO	30	60	4.8e+14	4.0	8.0
C_2H_5CN	5	275	1.9e+16	5.0	5.5		30	150	1.9e+15	25.0	9.0
	10	110	1.4e+15	13.0	4.0		15	110	1.7e+16	4.0	7.5
	25	65	3.0e+14	20.0	4.0		10	300	2.4e+16	4.0	7.5
CH_3NH_2	15	100	2.4e+14	4.0	6.0		10	250	7.7e+15	10.0	5.5
CH_3OH	30	50	2.4e+16	4.0	8.0	CH_3OCHO $v_t = 1$	15	100	1.1e+16	3.0	8.0
	15	110	2.4e+17	4.0	7.5	CH_2OCH_2	15	50	6.0e+13	3.0	7.5
	30	150	2.4e+15	25.0	9.0		15	50	1.2e+13	1.5	7.5
$^{13}CH_3OH$	30	50	2.4e+14	4.0	8.0	CH_3OCH_3	15	100	1.4e+16	3.0	7.5
	15	110	2.4e+15	4.0	7.5	CH_3COCH_3	10	100	1.8e+15	4.0	5.5
A-CH_3OH $v_t = 1$	15	110	1.2e+17	4.0	7.5	HNCO	30	60	6.0e+13	4.0	9.0
E-CH_3OH $v_t = 1$	15	110	1.2e+17	4.0	7.0		30	125	3.0e+14	25.0	6.0
C_2H_5OH	15	60	7.2e+14	4.0	8.0		15	110	4.8e+14	4.0	7.5
HCOOH	10	50	3.0e+14	3.0	7.5		10	225	8.4e+14	10.0	5.5
H_2CO	30	50	6.0e+14	25.0	6.0		5	300	6.0e+15	5.0	5.5
	15	50	6.0e+15	3.0	8.0	*NH_2CHO*	10	100	1.2e+14	3.0	7.0
	10	50	1.2e+15	10.0	5.5	NH_3	10	400	2.0e+16	30.0	8.0

Table 2
(Continued)

Species	Size ($''$)	T_{ex} (K)	N_{tot} (cm^{-2})	ΔV (km s^{-1})	V_{lsr} (km s^{-1})	Species	Size ($''$)	T_{ex} (K)	N_{tot} (cm^{-2})	ΔV (km s^{-1})	V_{lsr} (km s^{-1})
$H_2^{13}CO$	15	50	1.8e+14	3.5	9.5		10	300	1.2e+16	8.0	6.0
H_2CCO	10	100	1.8e+15	3.0	8.0	NH_2D	10	100	6.0e+14	8.0	6.0

Notes.

[a] The species in italic means their transitions are marginally detected or highly blended. The emission of SiO and its isotopologues is not modeled. See Section 5.2.4 for the fitting of C_2H_5CN $\upsilon 13/\upsilon 21$.

[b] The emission source size and T_{ex} for each spectral component are fixed (Section 4.2). The spectral modeling of this work is mainly used for line identification, and particular caution should be taken if the modeled parameters (e.g., N_{tot}) listed in Table 2 are used for comparison with results of other work.

[c] For species in vibrational state, to derive the column density, the partition function of the corresponding molecule accounting for all vibrational states is adopted. Thus, the column density should be interpreted as the column density of the corresponding molecule. If another emission source size is adopted, the column densities could be recalculated through multiplying the values listed here by a factor of $(size/size^{new})^2$.

The parameters for different species were basically independent. However, to reproduce the profiles of emission lines of isotopologues or species with similar chemical characteristics, we tend to adopt similar fixed values for their D and T_{ex}, and use a similar initial guess for their fitted parameters. For most species whose transitions have similar upper-level energies, the fitting result is not sensitive to T_{ex}. For those species, T_{ex} is manually adopted as 50, 100, 150, 200, or 300 K. We have also referred to the literature (Rizzo et al. 2017; Tercero et al. 2010) to guess the initial values of the fitted parameters. We try to model the spectrum with as few spectral components as possible. After each iteration of model fitting, we manually checked the fitting result to see whether there are line peaks, skewed line shoulders, or line wings that are obviously not well fitted. If so, we added a spectral component to fit them.

The spectra of different species are fitted separately. The species with strong lines are first fitted. For each of the rest species, the fitting procedure is conducted on the residual spectrum (the difference between the original spectrum and the modeled spectrum of all other fitted species). This procedure is iterated until all of the species are well fitted.

4.2.2. Fitting Results of Molecular Lines

All of the identified species except SiO and its isotopologues were modeled. The transition parameters of C_2H_5CN $v13/v21$ are not yet publicly available from the databases of JPL and CDMS, and we obtained those parameters from Endres et al. (2021) through private communication. We will discuss the fitting of C_2H_5CN $v13/v21$ in Section 5.2.4.

The spectrum of E-CH_3OH $v_t = 1$ cannot be well fitted with a T_{ex} of 100 K. Adopting T_{ex} as 110 K, the temperature of the compact ridge (Tercero et al. 2010), the spectrum of E-CH_3OH $v_t = 1$ can be better reproduced. It is consistent with the result of its rotational diagram (Figure 7), which yields a T_{ex} of 115 ± 5 K for E-CH_3OH $v_t = 1$. We adopted T_{ex} as 110 K to fit the corresponding spectral components of E-CH_3OH $v_t = 1$, A-CH_3OH $v_t = 1$, CH_3OH, and $^{13}CH_3OH$. The spectra of CH_3OCHO, HNCO, C_2H_3CN, and C_2H_5CN can be well fitted with the spectral components quoted from Rizzo et al. (2017) with T_{ex} unaltered. For CH_3OCHO and HNCO, the deviation between the fitted column densities of this survey and those of Rizzo et al. (2017) are smaller than 50%. However, for C_2H_3CN and C_2H_5CN, the fitted column densities of this survey are 3–10 times lower than the values of Rizzo et al. (2017). Only one line of CH_3CN is covered, and it is strong with a highly non-Gaussian shape. The fitting results of CH_3CN should be treated as rough estimations with large uncertainties.

The fitting results of the modeled parameters are listed in Table 2. For each species, we extracted the spectral segments that may contain emission of that species. Those spectral segments were then spliced together (referred to as the "spliced spectrum"). The spliced spectra for all fitted species are shown in Figures 8 and 9. For the transitions of most species, the deviations between the modeled intensities and the observed values are smaller than 10%. The spliced spectrum of NH_2D is an exception. NH_2D has two detected transitions (43,042 and 49,962 MHz), and those two lines cannot be simultaneously well reproduced.

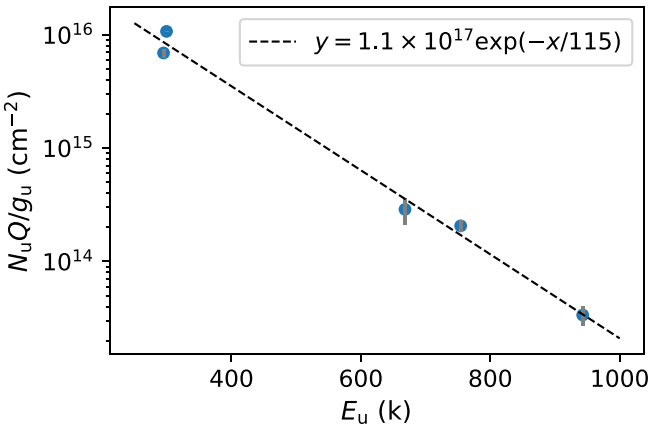

Figure 7. The rotational diagram of E-CH_3OH $v_t = 1$.

4.2.3. Groups of Spectral Components

The spectral components are divided into three groups in the velocity and line width (V_{LSR}–ΔV) space using the K-means algorithm (Lloyd 1982) implemented in SciPy,[16] as shown in Figure 10. The three groups are associated with three gas components of Orion KL: the plateau, the hot core, and the extended/compact ridge (Tercero et al. 2010; Rizzo et al. 2017). The median values of V_{LSR} of the three groups are 7 km s^{-1}, 6 km s^{-1}, and 8.5 km s^{-1}, respectively. The median values of ΔV of the three groups are 25 km s^{-1}, 8 km s^{-1}, and 3 km s^{-1}, respectively. Roughly, the line widths of spectral components in groups of the extended/compact ridge, hot core, and plateau are in the range of 1–5 km s^{-1}, 5–15 km s^{-1}, and 15–30 km s^{-1}, respectively. The kinetic temperature of the compact ridge, ~100 K, is higher than the value of the extended ridge, ~60 K (Tercero et al. 2010). However, most of the T_{ex} listed in Table 2 have quite large uncertainties, and thus it is difficult to explicitly assign a spectral component with $\Delta V < 5$ km s^{-1} to the compact ridge or the extended ridge.

For oxygen-bearing species, most of their spectral components (29/49) have $\Delta V <= 5$ km s^{-1} (Figure 10). It is expected since most of the oxygen-bearing species have spectral components originating from the extended/compact ridge. Thirty-eight percent (10/28) of the spectral components of sulfur-bearing species have $\Delta V > 15$ km s^{-1}. In contrast, for oxygen-bearing species, only 24% (12/49) of the spectral components have $\Delta V > 15$ km s^{-1}. Aldehyde-containing species and species with both sulfur and oxygen elements tend to have spectral components originating from the plateau (Table 2), and this supports a possible enhancement of these species by shocks (e.g., Feng et al. 2015; Lefloch et al. 2017; Liu et al. 2021).

5. Analysis and Discussion

5.1. RRLs

Figure 11 shows the comparison between the numbers of emission lines of this survey with and without detection by Rizzo et al. (2017). Forty-six of those RRLs were detected and spectrally resolved by Rizzo et al. (2017).

[16] https://pypi.org/project/scipy/

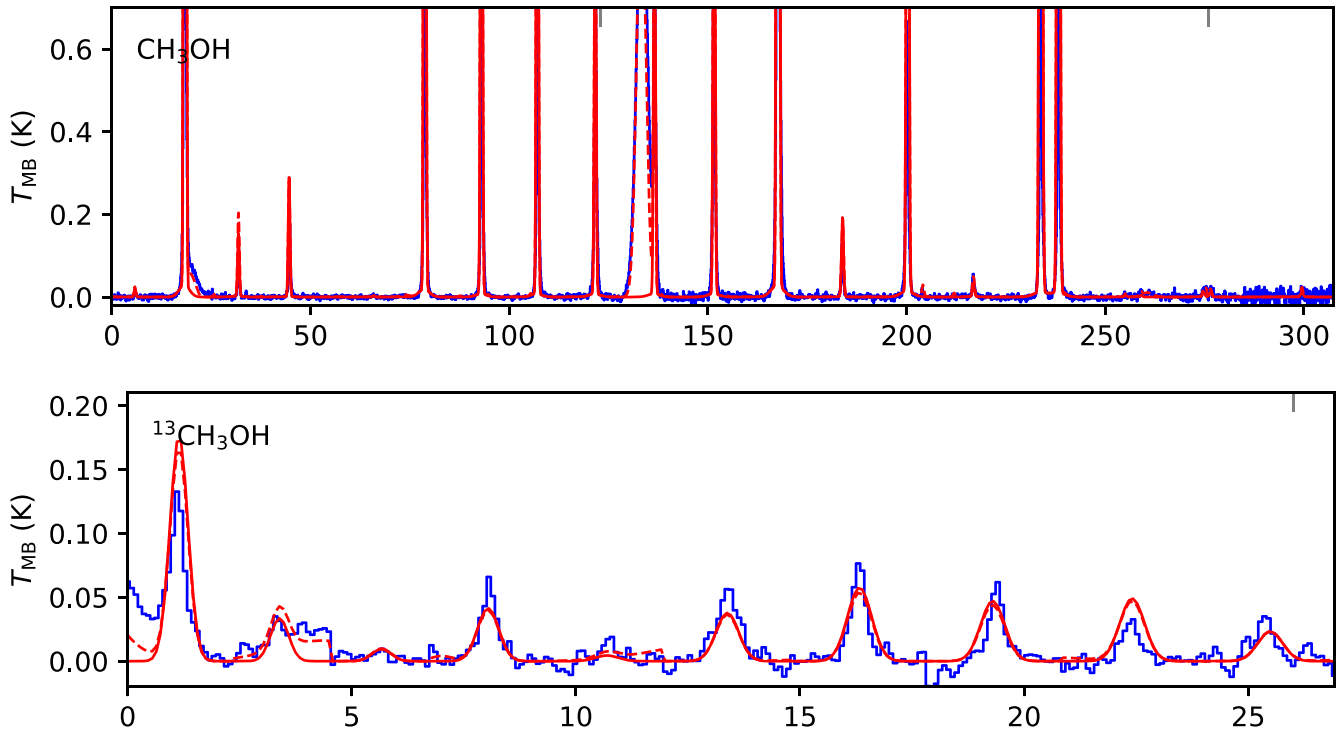

Figure 8. Model fitting for CH_3OH (upper panel) and $^{13}CH_3OH$ (lower panel) as an example. Spectra at different transitions are spliced together with segments marked by the gray ticks on the top axis. The *x*-axis is in units of megahertz with a channel width of 91.553 kHz (no smoothing applied). The solid red line represents the model fitting of the corresponding species, while the dashed line includes the contributions of all of the modeled molecular species (Table 2) and RRLs (see Section 4 for details). See Figure 9 for other species.

5.1.1. The Maximum Δn of Detected RRLs

Among the unblended hydrogen RRLs detected in this survey, H135π has the maximum Δn of 16. The maximum Δn of this survey is larger than the values of the *Q*-band survey of Rizzo et al. (2017) and the radio *K*-band (1.3 cm) survey of Gong et al. (2015). The maximum Δn detected by Rizzo et al. (2017) and Gong et al. (2015) was 11 for both. For spectrally resolved helium RRLs in this survey, the maximum Δn is 7, and it is also higher than the values of 4 detected by Rizzo et al. (2017) and Gong et al. (2015). The carbon RRLs detected by Gong et al. (2015) are all carbon α lines highly blended with helium RRLs. Only two carbon RRLs (C52α and C53α) were firmly detected and resolved by Rizzo et al. (2017). On the contrary, 10 RRLs of carbon are resolved in this survey, including the C81γ with a Δn of 3 (Figure 12). Thanks to the higher sensitivity and wider frequency coverage of this survey, this work has more than doubled the number of detected RRLs, particularly those with larger Δn, in the *Q* band compared with Rizzo et al. (2017).

5.1.2. Intensity Ratios and Dynamics of RRLs

Benefiting from a large number of RRLs detected in this survey, we can estimate the abundance ratio of He/H via the intensity ratio between their RRLs with the same n and Δn:

$$y = \frac{N(\mathrm{He})}{N(\mathrm{H})} \sim \frac{1}{R^{1/3}} \times \frac{\int T_\nu(\mathrm{He})d\nu}{\int T_\nu(\mathrm{H})d\nu}. \quad (12)$$

Here, $\int T_\nu(\mathrm{X})d\nu$ is the integrated intensity of the RRL of X, and the R is the volume ratio between the ionized regions of He and H. If the R value is adopted as unity considering the similarity between the line widths of hydrogen and helium RRLs (Table 3), the inferred mean value of y is 8.4% with a standard deviation of 0.2% (Figure 13).

The y-value derived here is consistent with the result of global fitting described in Section 4.1.2. It is also consistent with the values of $(8.7 \pm 0.7)\%$ derived by Gong et al. (2015), $(8.3 \pm 1.2)\%$ by Rizzo et al. (2017), and $(8.8 \pm 0.6)\%$ by Baldwin et al. (1991) derived based on optical observations. The value of y seems to be compatible with the value of 8.3% due to Big Bang nucleosynthesis (Olive & Skillman 2004) and lower than the solar value, 9.8% (Wilson & Rood 1994). However, if an R value of 0.6 is adopted (Copetti & Bica 1983), the derived value of y is 10%, much closer to the solar value.

The velocities of unblended hydrogen, helium, and carbon RRLs are shown in the lower panel of Figure 13. The velocities of hydrogen and helium RRLs at different frequencies are consistent with a value of -3 ± 1.5 km s^{-1}. The velocities of carbon RRLs are $\sim +9 \pm 1$ km s^{-1}. The computed velocities are compatible with previous results that the hydrogen and helium RRLs arise from the M42, while the carbon RRLs originate from the PDR between M42 and the associated molecular clouds (the Orion Bar; see Cuadrado et al. 2015; Gong et al. 2015; Rizzo et al. 2017).

5.2. Molecular Species

As shown in Figure 11, among the 371 molecular transitions detected and identified by this survey, 329 are unblended and only 108 of them have been firmly detected and identified by Rizzo et al. (2017). Those molecular transitions belong to 53 species—most of them are sulfur-bearing species, oxygen-bearing organic molecules, nitrogen-bearing species (cyanopolyynes, N-bearing COMs, and NH_3), and their isotopologues. Among the 53 detected species, 32 were firmly detected by Rizzo et al. (2017).

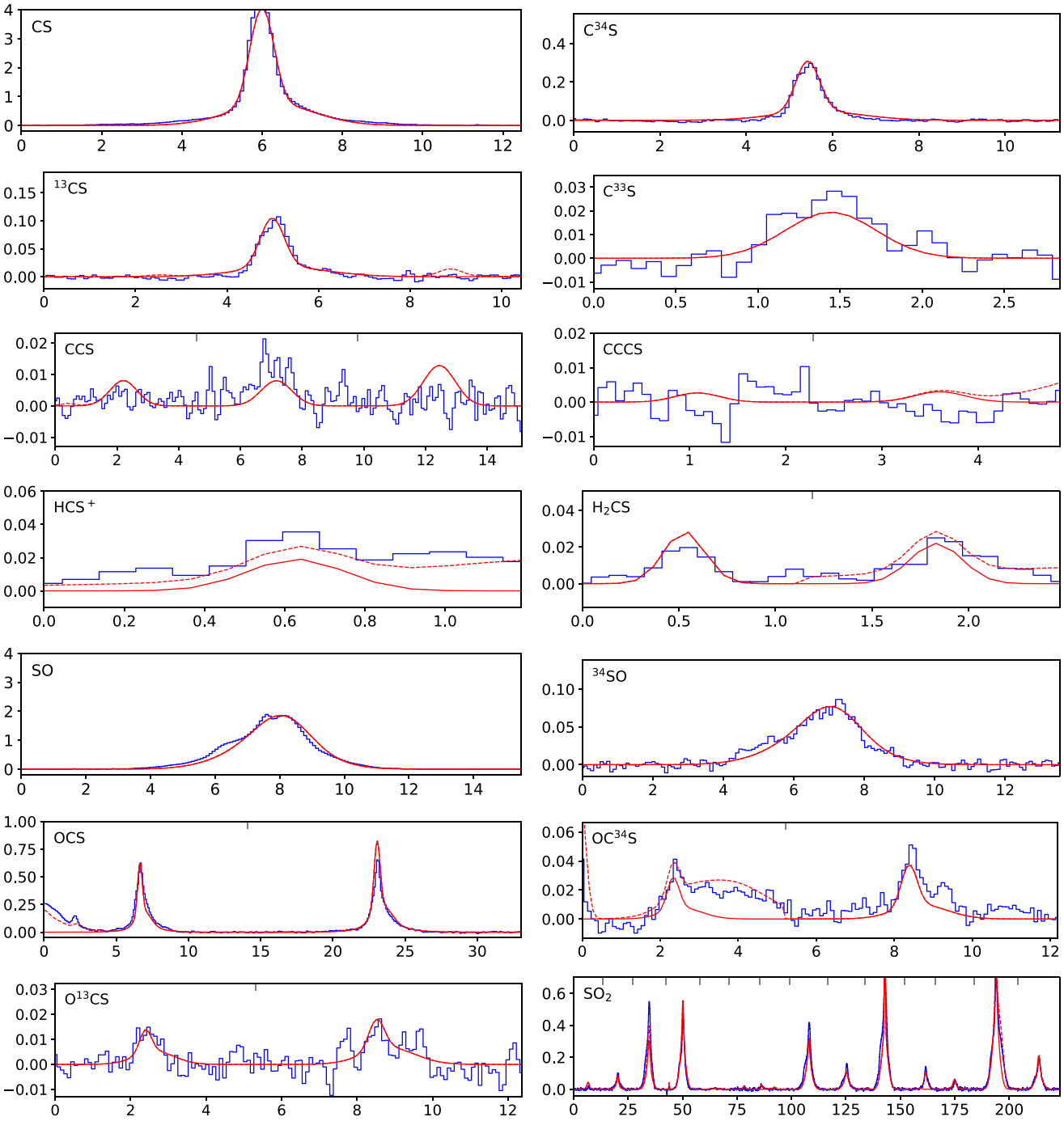

Figure 9. Model fitting for different species. Continued from Figure 8. Note: In each panel, the spectrum between two neighboring upper ticks is an independent frequency segment containing transitions of the corresponding species. The solid red line represents the model fitting of the corresponding species, while the dashed line includes the contributions of all modeled molecular species (Table 2) and RRLs (see Section 4 for details). The *x*-axis is in units of megahertz. Each spectrum has been smoothed to a spectral resolution of 183 kHz.

The other 21 species were not firmly detected by Rizzo et al. (2017), including the tentatively detected NH_2CHO.

5.2.1. Sulfur-bearing Species

Sulfur-bearing molecules (e.g., H_2S, SO, SO_2, CS, OCS, and H_2CS) have been detected in various star-forming environments (e.g., Turner et al. 1973; Luo et al. 2019; Wu et al. 2019b). Thirteen kinds of isotopologues of sulfur-bearing molecules are detected in this survey. Among them, five species were not confirmed by Rizzo et al. (2017).

The comparison between the HCS^+ spectra of this survey and that of Rizzo et al. (2017) is shown in Figure 14. The narrow emission line of HCS^+ is overlapped with the broad emission of C_2H_5CN. Although Rizzo et al. (2017) marked this line as a blended line of HCS^+ and C_2H_5CN, the broad emission of C_2H_5CN cannot be seen in their spectrum. This further reduces the degree of confidence of the possible HCS^+ emission feature with a limited signal-to-noise ratio (S/N). In the spectrum of this

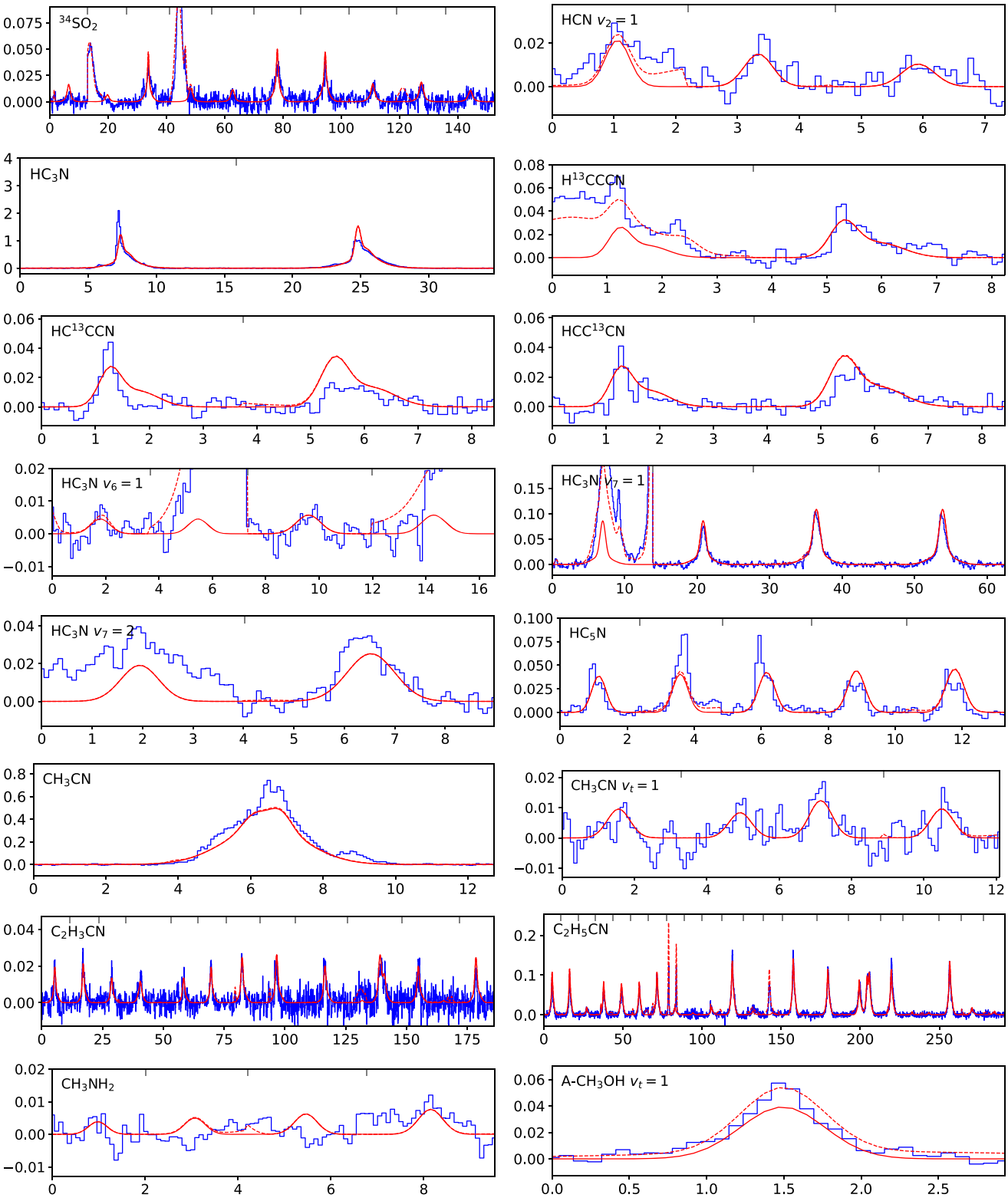

Figure 9. (Continued.)

survey, the emission of HCS^+ and C_2H_5CN can be spectrally resolved. Our survey has higher sensitivity and smaller beam size, and this may make our survey more sensitive to emission of compact sources such as the emission regions of COMs.

Two transitions of H_2CS were detected in this survey. The line width of H_2CS is consistent with the value of HCS^+ (see Figure 9 and Table 2). This implies that H_2CS and HCS^+ may originate from similar emission regions and have tight chemical

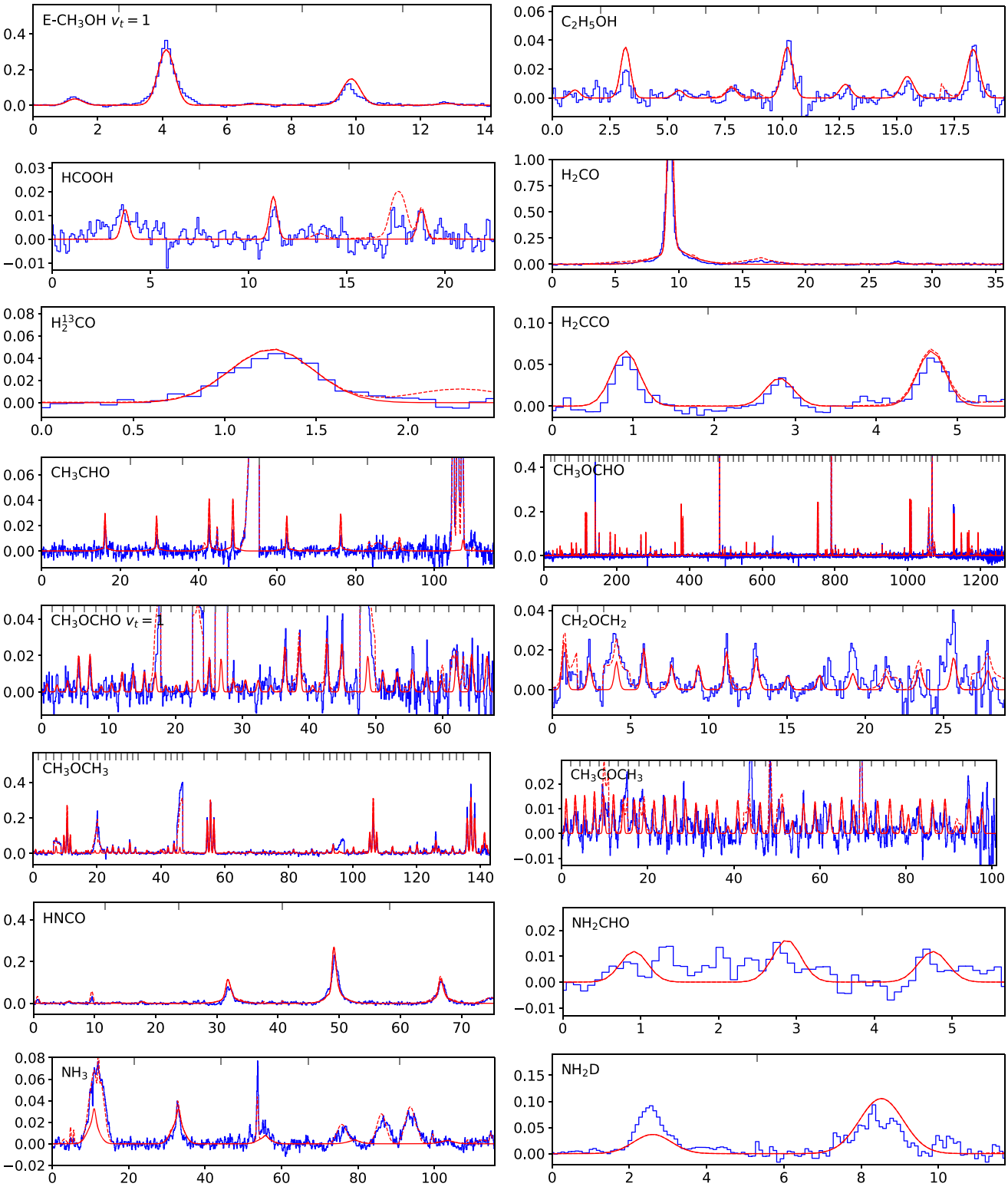

Figure 9. (Continued.)

correlation, through reactions such as (McElroy et al. 2013)

$$\begin{aligned} CH_2^+ + OCS &\rightarrow H_2CS^+ + CO \\ CH_2^+ + OCS &\rightarrow HCS^+ + HCO \end{aligned}. \quad (13)$$

We note that the emission feature identified as the $J = 8$–7 of C_3S by Rizzo et al. (2017) cannot be seen in the spectrum of this survey (Figure 14). There is also no emission feature at C_3S $J = 7$–6 (40,465 MHz). Since $J = 8$–7 is the only line of C_3S detected by Rizzo et al. (2017) with limited S/N, the contribution of noise cannot be ignored. The column density of C_3S may be much lower than the value estimated by Rizzo et al. (2017). However, since our observation has a smaller beam size, it cannot be excluded that the C_3S emission detected

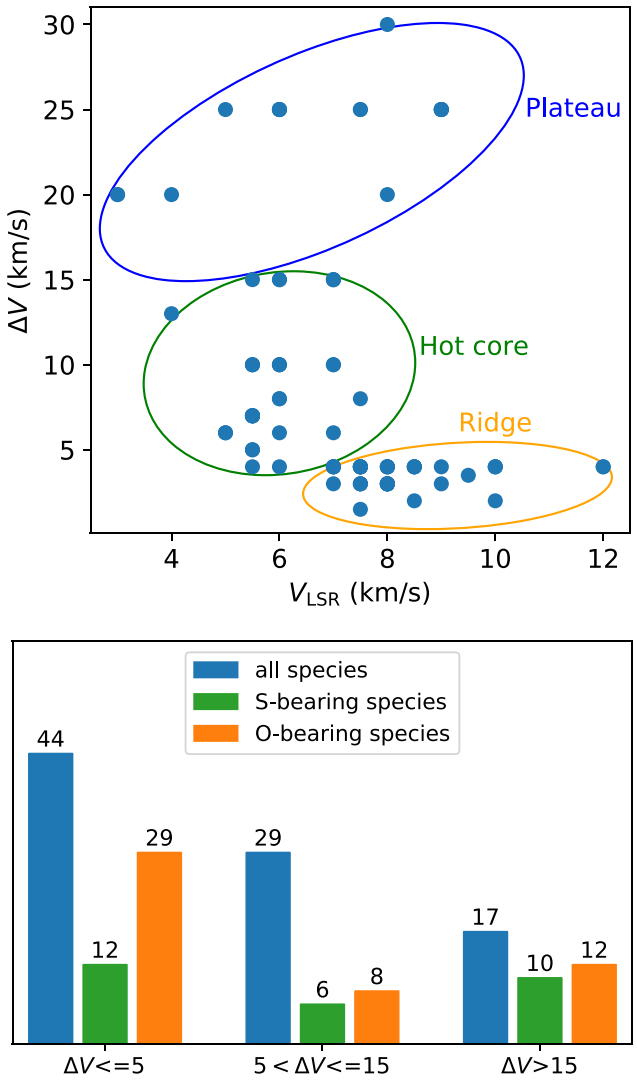

Figure 10. Upper: groups of spectral components (Table 2) by K-means (Section 4.2.3). Lower: the number of spectral components with ΔV (in units of kilometers per second) in three different ranges.

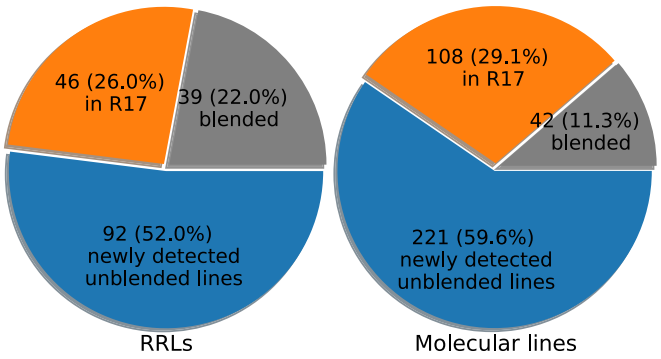

Figure 11. Pie diagrams to compare the number of molecular lines and RRLs of this survey with and without detection by R17 (Rizzo et al. 2017).

by Rizzo et al. (2017) originates from regions uncovered by the beam of this survey. The CCS emission identified by Rizzo et al. (2017) is also not detected or only marginally detected in this survey (Figure 9).

One transition of $O^{13}CS$ is observed by Rizzo et al. (2017) and two by this survey. The emission of $O^{13}CS$ is marginally

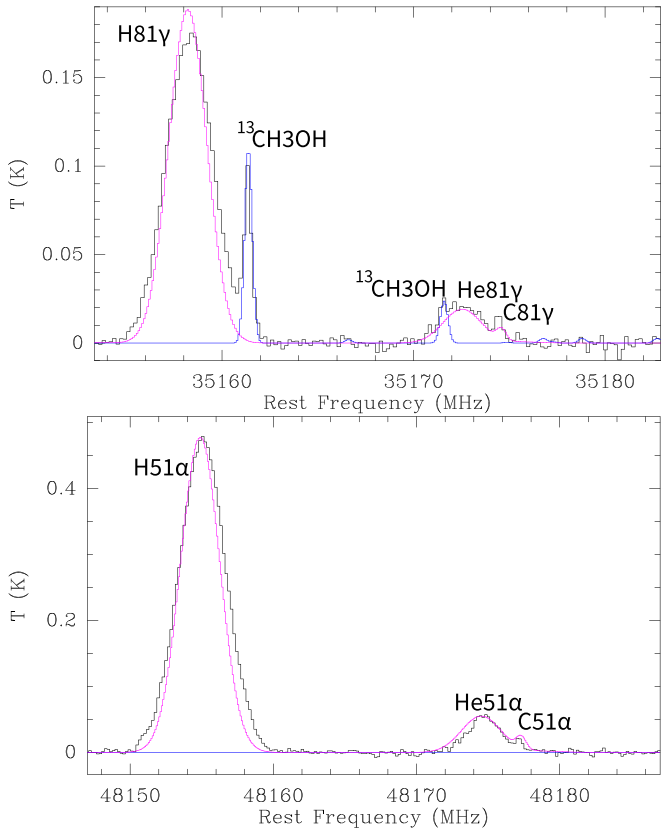

Figure 12. Upper: the black line is the observed 81γ lines of H, He, and C. It has been smoothed to a channel width of 183 kHz (1.56 km s^{-1}). The purple line is the modeled RRLs, and the blue line is the modeled molecular lines (Section 4). Lower: the same as the upper panel but for the 51α lines.

detected in this survey and Rizzo et al. (2017). For our survey, since there are weak emission features at both of its two transitions, $O^{13}CS$ is marked as a detected species.

5.2.2. *Oxygen-bearing Organic Molecules*

In total, 15 kinds of oxygen-bearing organic species are detected in this survey. We use three velocity components to fit the emission of CH_3OH, including two narrow components with $\Delta V = 4$ km s^{-1} and a broad component with $\Delta V = 25$ km s^{-1} (Table 2). The wide wings of $^{13}CH_3OH$ have not been obviously detected; thus, the broad component ($\Delta V = 30$ km s^{-1}) has not been reused from CH_3OH to fit the spectrum of $^{13}CH_3OH$. The spectrum of $^{13}CH_3OH$ can be well modeled when adopting the column densities of $^{13}CH_3OH$ as 0.01 times the values of the two narrow components of CH_3OH (see Figure 8). If the CH_3OH and $^{13}CH_3OH$ have identical emission regions, it implies that the abundance ratio between $^{13}CH_3OH$ and CH_3OH can be estimated as 0.01. For E-CH_3OH $v_t = 1$ and A-CH_3OH $v_t = 1$, the model parameter of CH_3OH can also be applied to them without any modification to reproduce their spectra, assuming that the A-type and E-type of CH_3OH have equal abundances. C_2H_5OH is also detected in this survey. The model fitting gives an abundance ratio between C_2H_5OH and CH_3OH of 0.003.

Apart from H_2CO and CH_3OCHO, which have been detected by Rizzo et al. (2017), the molecules containing an aldehyde group detected in this survey include $H_2^{13}CO$, H_2CCO, and CH_3CHO. The abundance ratio between $H_2^{13}CO$

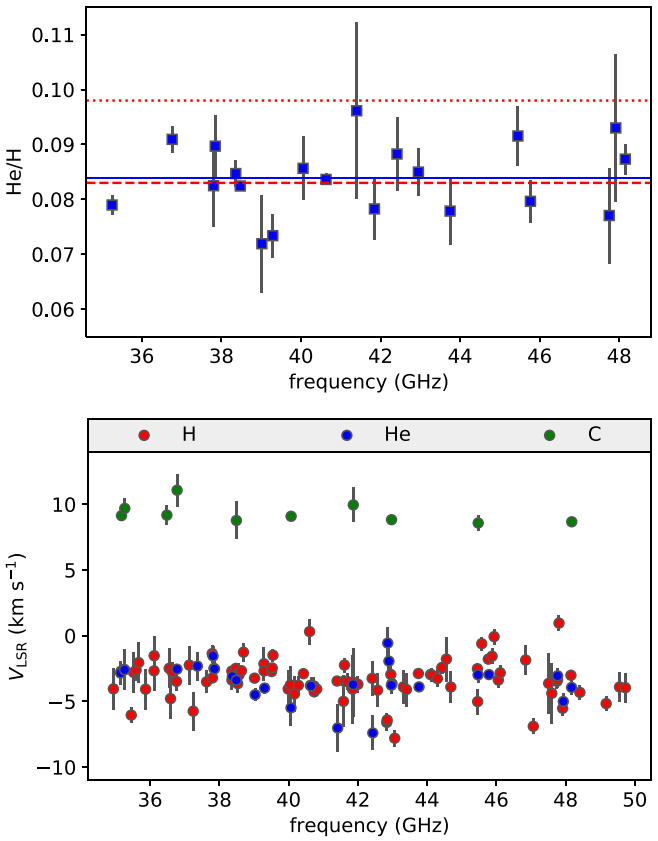

Figure 13. Upper: the intensity ratios between RRLs of He and H. The red dotted and dashed lines represent the He/H abundance ratio of 8.3% due to Big Bang nucleosynthesis (Olive & Skillman 2004) and the solar value ∼9.8% (Wilson & Rood 1994), respectively. The blue solid line is the mean value of the data. Lower: the V_{LSR} of unblended RRLs of H, He, and C derived by Gaussian fittings.

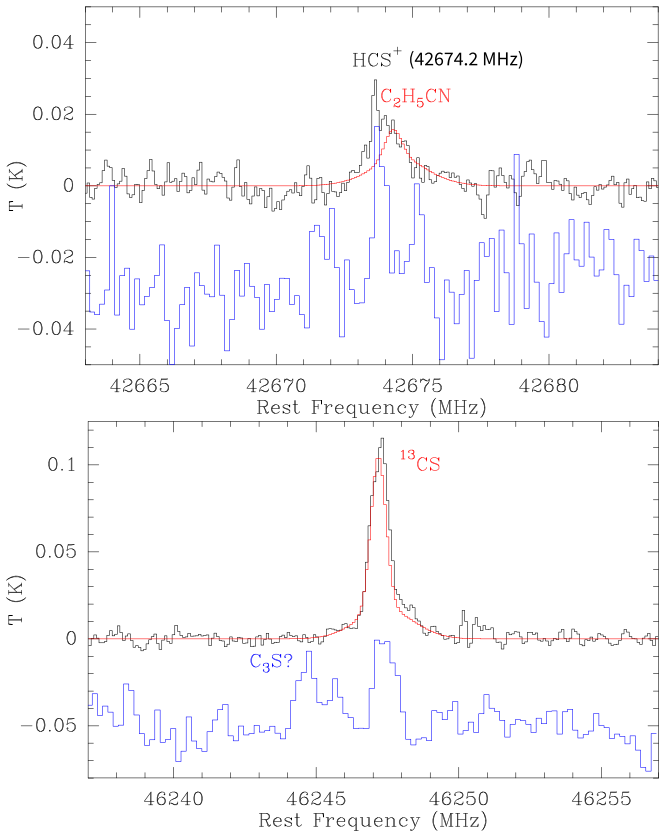

Figure 14. In both panels, the black lines are the spectra detected in our survey, and the blue lines are the spectra of Rizzo et al. (2017). In the upper panel, the red line is the model fitting of C_2H_5CN. In the lower panel, the red line is the model fitting of ^{13}CS. The small peak near 46,245 MHz (blue line) was identified as C_3S $J = 8$–7 by Rizzo et al. (2017). See Section 5.2.1 for the discussion about the emission features of C_3S.

and H_2CO is estimated as 0.02, and the value between CH_3CHO and H_2CO is 0.06. The first vibrationally excited state of CH_3OCHO ($v_t = 1$) was detected by Rizzo et al. (2017) through stacking faint lines; most of them are near the detection limit. In our survey, more than 10 lines of CH_3OCHO $v_t = 1$ have been detected with significant S/Ns (Figures 15 and 9).

Three lines of HCOOH (formic acid) are detected in this survey, with a velocity of ∼7.5 km s^{-1}. Liu et al. (2002) observed the HCOOH lines at 225 GHz and 262 GHz using the Berkeley–Illinois–Maryland Association array, and the line emission was found to peak in the velocity range of 6.9–8.4 km s^{-1}. Near the compact ridge, the HCOOH emission was spatially resolved by Liu et al. (2002), showing a partial shell morphology. If an emission size of 10″ and an excitation temperature of 60 K is adopted, the fitting of Q-band lines of this survey gives an HCOOH column density of 3.0×10^{14} cm^{-2} (Table 2). This is consistent with the value of 4.8×10^{14} cm^{-2} derived by Liu et al. (2002) adopting an excitation temperature of 62 K.

Interstellar acetone (CH_3COCH_3) is a COM that has been previously detected in several hot cores and low-mass protostars (e.g., Combes et al. 1987; Jørgensen et al. 2011; Friedel & Widicus Weaver 2012; Zou & Widicus Weaver 2017). Toward the Orion KL, the transitions of CH_3COCH_3 were not detected or only marginally detected by Rizzo et al. (2017). Six CH_3COCH_3 lines were identified by Goddi et al. (2009). In this survey, more than 10 weak emission features were assigned to transitions of CH_3COCH_3 (see Table 3). However, most of them are marginally detected. We stacked the lines of CH_3COCH_3 to justify the detection of CH_3COCH_3 in Section 5.2.6.

5.2.3. Cyanopolyynes

Cyanopolyynes ($HC_{2n+1}N$) are chemically young species, and they are usually detected in cold cores, cold/warm ambient gas of star-forming regions, and the envelopes of late-type carbon stars (e.g., Dickens et al. 2001; Esplugues et al. 2013a; Agúndez et al. 2017; Liu et al. 2021). The vibrational levels of HC_3N are mainly excited by mid-IR radiation (de Vicente et al. 2000), and it also makes HC_3N a good tracer of hot cores (Turner 1971; Liu et al. 2020).

For the isotopologues of HC_3N (including $H^{13}CCCN$, $HC^{13}CCN$, and $HCC^{13}CN$), the observations of Rizzo et al. (2017) only covered their $J = 5$–4 transitions. This survey covers the transitions of both $J = 4$–3 and $J = 5$–4. Thus, we can better constrain the emission model (Section 4.2) of HC_3N and its isotopologues. The modeled emission of $H^{13}CCCN$, $HC^{13}CCN$, and $HCC^{13}CN$ with identical column densities and excitations approximately reproduces the observations for all of their detected transitions (Figure 9). We speculate that the ion-molecule reactions are preferred to produce HC_3N in Orion KL, since they may not lead to significant divergence of abundance among different isotopologues of HC_3N as compared with the neutral-neutral reactions (Taniguchi et al. 2016).

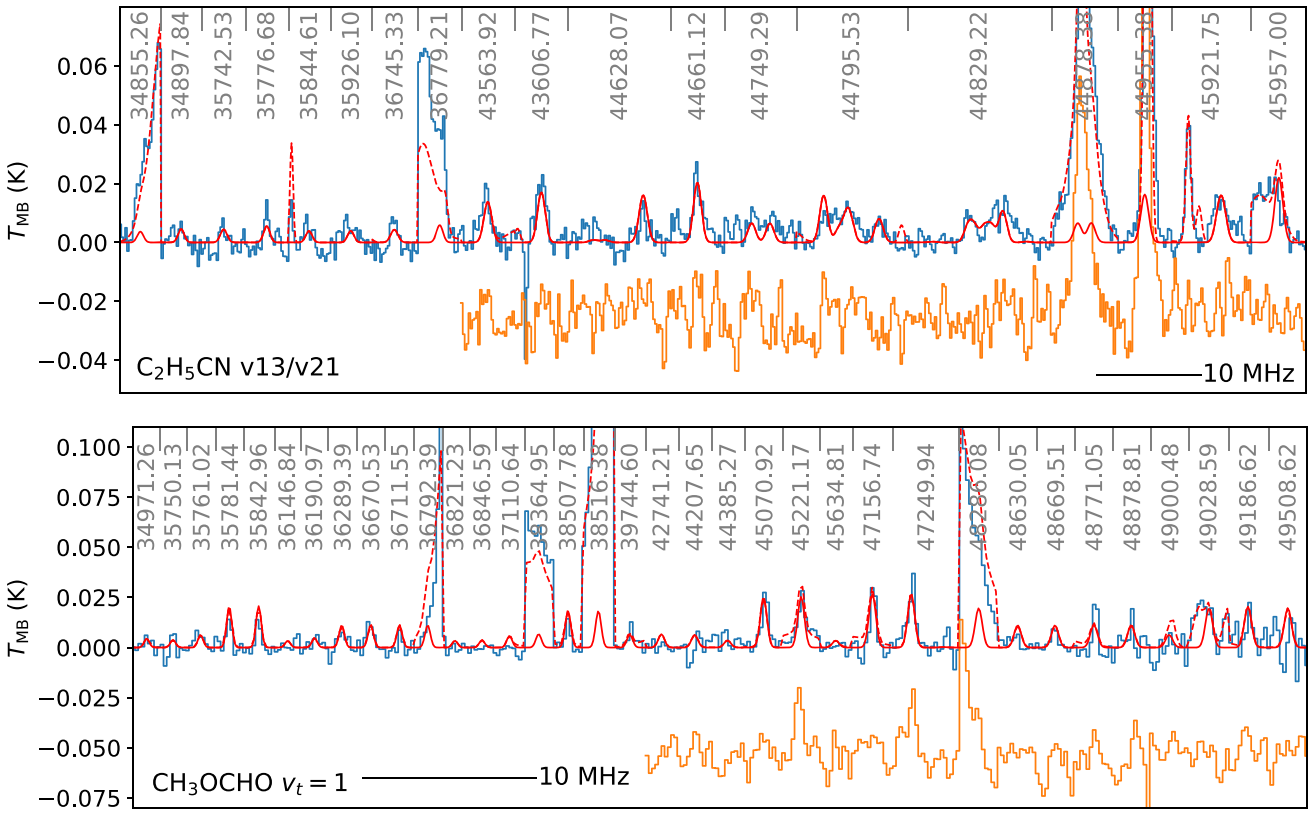

Figure 15. The "spliced" spectra of C_2H_5CN $\upsilon 13/\upsilon 21$ (upper panel) and CH_3OCHO $\upsilon_t = 1$ (lower panel). The blue and orange lines are spectra from this survey and Rizzo et al. (2017), respectively. The spectra have been smoothed to have a spectral resolution of 183 kHz (twice the spectral resolution of this survey). The center frequencies of each segment are shown on the top axis. The red line is the result of model fitting. The red dashed line includes the contributions of all of the fitted molecular species (Table 2) and RRLs (see Section 4 for details). The unsmoothed version for CH_3OCHO $\upsilon_t = 1$ can be found in Figure 9.

Only two vibrationally excited HC_3N transitions were firmly detected in Rizzo et al. (2017). In this survey, at least two unblended transitions are detected for each of the three vibrational levels ($\upsilon_6 = 1$, $\upsilon_7 = 1$, and $\upsilon_7 = 2$) of HC_3N. Five transitions of HC_5N are also detected in this survey.

5.2.4. C_2H_5CN $\upsilon 13/\upsilon 21$

Ten lines of C_2H_5CN $\upsilon 13/\upsilon 21$ are detected in this survey. Among those lines, nine are spectrally resolvable and they are marked by red strips in Figures 5 and 4. Those lines are all undetected or only marginally detected (with $S/N < 3$) by Rizzo et al. (2017). To identify those lines, we privately communicated with the authors of Endres et al. (2021) to obtain the transition parameters (rest frequency, E_u, A_{ij}, and g_u) of transitions of C_2H_5CN $\upsilon 13/\upsilon 21$ within 34.8–50 GHz. Emission lines corresponding to those transitions are clearly detected in our survey (Figure 15). We modeled them using the method described in Section 4.2. The modeled spectrum is consistent with that observed in this survey, as shown in the upper panel of Figure 15. A T_{ex} of 50 K is assumed to model the spectrum of C_2H_5CN $\upsilon 13/\upsilon 21$, although T_{ex} cannot be well constrained since all of the detected transitions have similar E_u. The line width is fitted as 6.5 km s^{-1}. The column density of C_2H_5CN $\upsilon 13/\upsilon 21$ is undecided since we do not know the partition function.

The in-plane bending vibration $\upsilon 13 = 1$ and torsional state $\upsilon 21 = 1$ of C_2H_5CN (Daly et al. 2013) have been detected toward Sgr B2(N-LMH) by Mehringer et al. (2004) with rest frequencies ranging from 100–270 GHz. C_2H_5CN in vibrationally excited states has also been identified in Orion KL by Daly et al. (2013) from the data of an IRAM millimeter survey (Tercero et al. 2011). Rizzo et al. (2017) tried to search for signals of those transitions in the Q-band spectrum of their survey, but they failed to find signals with intensities higher than 3σ. The vibrationally excited states ($\upsilon 13/\upsilon 21$) of C_2H_5CN in the Q band are for the first time firmly detected in this survey.

5.2.5. HCN $\upsilon_2 = 1$ and NH_3

HCN in the vibrational state ($\upsilon_2 = 1$) is detected in their direct l-type lines in this survey (Figure 9). HCN $\upsilon_2 = 1$ is a vibrationally bending mode with a ground state energy of 1024.4 K (Radford & Kurtz 1970; Rolffs et al. 2011; Bruderer et al. 2015). If HCN in the vibrational state is thermally excited, an HCN column density of 1.8×10^{17} cm^{-2} is derived with an assumed excitation temperature of 200 K and an emission size of 10″. It is consistent with near-infrared observations toward the Orion KL using the Short Wavelength Spectrometer of Infrared Space Observatory (Boonman et al. 2003), where an HCN column density of $\sim 5 \times 10^{16}$ cm^{-2} was derived from the vibrational emission band of HCN at 14.05 μm, adopting a Doppler line width of 5 km s^{-1} and an excitation temperature of 275 K.

Three transitions of NH_3 are detected, including the inversion lines of (14,14), (15,15), and (16,16). The (14,14) is highly blended with the hydrogen RRLs and the emission of

CH_3OCH_3. The (15,15) is lightly blended with the emission of E-CH_3OCHO, which has a much narrower line width and contributes no more than 10% intensities. The (16,16) is close to a line feature of HC_5N, and it is easy to separate them through Gaussian fitting. The emission of NH_3 lines is modeled by two components with line widths of 8 and 30 km s^{-1}. The emission of NH_3 is necessary to reproduce the observed spectrum at the frequencies of the three transitions. Thus, we consider NH_3 as a detected species. The narrower component has a line width consistent with the value for NH_2D (8 km s^{-1}). It is also consistent with the result of Wilson et al. (1993), who detected inversion lines of NH_3 up to (14,14) with a line width of ~10 km s^{-1}. The detection of NH_3 (15,15) and (16,16) in this survey pushes the upper-level energy of NH_3 emission lines detected toward Orion KL upward to >2000 K.

5.2.6. Stacking Lines of CH_3COCH_3

We stacked the emission of CH_3COCH_3 to improve the S/N and to consolidate the detection of CH_3COCH_3 of this survey. To avoid bias, all of the unblended transitions of CH_3COCH_3 (including both the detected ones and undetected ones) were stacked. We first calculate the relative intensity (r_i) of the $i_{\rm th}$ transition through Equation (10) assuming a $T_{\rm ex}$ of 100 K. The r_i is then normalized to have a maximum value of 1. Then, the spectrum of each segment was rescaled through multiplying a factor of $1/r_i$ to make them have equal expected intensities. Obviously, the noise has also been amplified by a factor of $1/r_i$, simultaneously. The rescaled spectra are then averaged to get the stacked spectrum, with a weight of r_i^2 for each. These procedures are equivalent to directly stacking up the original spectra weighted by $r_i/\sum_1^N r_i^2$. Here, N is the number of stacked transitions. We use $\sum_i^N r_i^2$ to represent the effective number of stacked transitions ($N_{\rm eff}$). If $N_{\rm eff}$ is small, bias arising from possible noise spikes at a few transitions may be unignorable. The $N_{\rm eff}$ is 11 and 9.5 for CH_3COCH_3 of this survey and of Rizzo et al. (2017), respectively. Thus, the stacking procedure is valid for CH_3COCH_3. The stacked line of CH_3COCH_3 of our survey shows an obvious emission feature (Figure 16). In contrast, the stacked line of CH_3COCH_3 of Rizzo et al. (2017) only has a weak emission feature lower than 3σ. We also stack a group of spectral segments, with each of the N segments having a rest frequency randomly chosen within the unblended frequency ranges. The randomly stacked spectrum shows no emission feature as expected. Thus, the weak emission features we assign to CH_3COCH_3 should be real, and CH_3COCH_3 is considered a detected species.

5.3. SiO Emission

5.3.1. Overall Description of SiO Emission

The upper panel of Figure 17 shows the $J=1$–0 spectra of SiO and its isotopologues (SiO $\upsilon=0$, SiO $\upsilon=1$, SiO $\upsilon=2$, ^{29}SiO $\upsilon=0$, and ^{30}SiO $\upsilon=0$) detected in this survey. Overall, the line shapes agree with the single-dish results presented by Goddi et al. (2009) and Rizzo et al. (2017). The $\upsilon=0$ lines of ^{29}SiO and ^{30}SiO are broad and smooth, while the spectrum of SiO $\upsilon=0$ shows narrow features (Figure 17). This is consistent with previous results that the emission of SiO $\upsilon=0$ is part maser and part thermal (Chandler & de Pree 1995; Goddi et al. 2009).

SiO $\upsilon=1$, 2 transitions are known to have been inverted since their discovery (Buhl et al. 1974; Thaddeus et al. 1974). The SiO $\upsilon=1$ of this survey and Goddi et al. (2009) have a nearly identical shape. This implies that the shape of SiO $\upsilon=1$ may have not obviously changed during the past 10 yr under the single-dish view. However, the bright and very narrow feature in the $\upsilon=2$ line at ~−1.4 km s^{-1} reported by Rizzo et al. (2017) cannot be seen in the spectra of Goddi et al. (2009) and this survey. The velocity component of SiO $\upsilon=2$ with a $V_{\rm LSR}$ of ~22 km s^{-1} has a much lower intensity compared with that of Goddi et al. (2009). The SiO $\upsilon=2$ seems to have experienced a more significant change than SiO $\upsilon=1$ during the past 10 yr.

5.3.2. A Very Narrow and Weak SiO Maser Component

There is a very narrow (spectrally not well resolved) and weak (~0.1 K) emission feature at $V_{\rm LSR}\sim-22$ km s^{-1} in the SiO $\upsilon=1$ spectrum (Figure 17). We have conducted observations covering this line on three different days adopting different frequencies of the LO, and this narrow and weak feature was detected in all sets. In the spectrum of SiO $\upsilon=2$, a broader feature was detected at a similar velocity (Figure 17). Thus, we identify the narrow and weak emission feature in the SiO $\upsilon=1$ spectrum as a narrow velocity component of SiO $\upsilon=1$.

5.4. Future Aspects

We took full use of the Q-band receiver of TMRT to search for emission lines of Orion KL under a sensitivity on the order of millikelvin. This survey proves that the TMRT is sensitive and stable enough to conduct deep line surveys. In this work, we have only displayed some preliminary results of this survey. More detailed scientific analysis and modeling will be conducted in future work. Further, we plan to make deeper Q-band integrations toward Orion KL using the TMRT in the near future, aiming to improve the S/Ns of newly detected transitions, to confirm the weak or blended emission features detected in this survey, and to search for the emission of new species. We also plan to extend our survey to other sources including SgrB2 and G010.47+0.03, and to other frequency bands available by TMRT, especially the Ka band, which could fill the gap between the K band and Q band.

6. Summary

We have conducted a line survey toward the Orion KL using the Q-band receiver of TMRT, covering a frequency range of 34.8–50 GHz. So far, this survey is the most sensitive wide-band Q-band survey toward the Orion KL. Compared with the survey of Rizzo et al. (2017), this survey extends the frequency coverage from 41.5–50 GHz to 34.8–50 GHz with sensitivities and spectral resolution two times better, on average. The main results of this survey include:

1. In total, 597 emission features were extracted from the Q-band spectrum of Orion KL. Gaussian fitting was applied to those emission features. Among them, 177 RRLs are identified, including 126, 40, and 11 RRLs corresponding to hydrogen, helium, and carbon, respectively. Further, 371 molecular transitions are identified, containing 330 unblended ones. The detected molecular transitions come from 53 species (including isotopologues and molecules in different vibrational levels). The thermal lines were then fitted with a radiative transfer model to reproduce the observed spectrum and reaffirm the line identification.

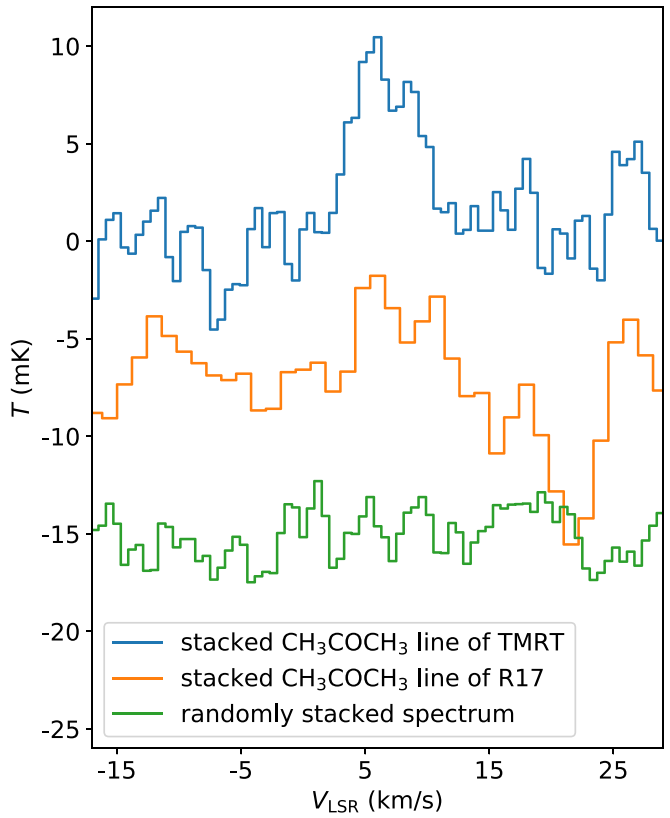

Figure 16. The blue and orange lines are the stacked lines of CH_3COCH_3 of our survey and Rizzo et al. (2017), respectively. The green line is stacked from randomly chosen segments of our spectrum. See Section 5.2.6 for details.

2. For RRLs, the EM of the H II region is fitted to be 3.9×10^6 cm^{-3} pc with an intensity ratio between He/H of 8.4%. The maximum Δn of unblended RRLs is 16 for hydrogen, 7 for helium, and 3 for carbon. The carbon RRLs are confirmed to originate from PDR regions with a $V_{\rm LSR} \sim 9$ km s^{-1}. The EM of the PDR region is estimated to be 3.9×10^3 (1.8×10^2) cm^{-6} pc, if an electron temperature of 2000 (300) K is assumed.
3. The line shape of the SiO $\upsilon = 1$ maser may have not obviously changed since Goddi et al. (2009), while the $\upsilon = 2$ maser tends to be more time-varying in the past 10 yr. A very narrow (spectrally not well resolved) and weak (∼0.1 K, more than 1000 times lower than the main peak) emission feature of SiO $\upsilon = 1$ is detected at $V_{\rm LSR} \sim -22$ km s^{-1}.
4. The detected molecular species are mainly cyanopolyynes, sulfur-bearing species, and oxygen-bearing organic molecules. Twenty-one of the 53 detected species have not been firmly detected by Rizzo et al. (2017), including species such as H_2CS, HCOOH, C_2H_5OH, $H_2^{13}CO$, H_2CCO, CH_3CHO, CH_2OCH_2 (ethylene oxide), HCN $\upsilon_2 = 1$, CH_3OCHO $\upsilon_t = 1$, and C_2H_5CN $\upsilon 13/\upsilon 21$. The transitions of CH_3COCH_3 are stacked to confirm the detection of CH_3COCH_3. The vibrationally excited states of C_2H_5CN in the Q band are for the first time firmly detected in this survey. The detection of NH_3 (15,15) and (16,16) in this survey pushes the upper-level energy of NH_3 emission lines detected toward Orion KL upwards to >2000 K.

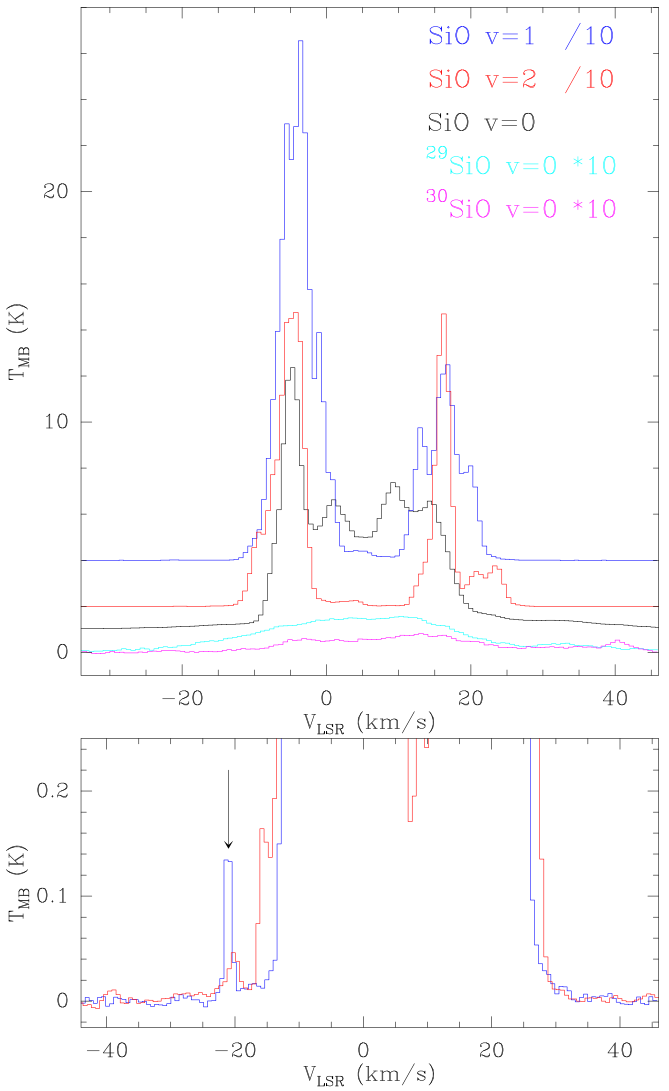

Figure 17. Upper: the spectra of SiO and its isotopologues. Lower: zoomed-in region of the spectra of SiO masers. The spectra of SiO $\upsilon = 1$ and $\upsilon = 1$ in the lower panel have not been divided by 10 as in the upper panel. The black arrow marks the weak and narrow feature beside the main features of SiO $\upsilon = 1$ (blue) and $\upsilon = 2$ (red).

This is the first systematic line survey of the TMRT, using its Q-band receiver and targeting on Orion KL. In this work, we have only displayed some preliminary results of this survey. More detailed scientific analysis, modeling, and further follow-up surveys will be conducted in future work.

We wish to thank the staff of the Tianma 65 m for their help during the observations. X.L. acknowledges support from NSFC Nos. 12203086 and 12033005. T.L. acknowledges support from the National Natural Science Foundation of China (NSFC) through grant Nos. 12073061 and 12122307, the international partnership program of Chinese Academy of Sciences through grant No. 114231KYSB20200009, the Shanghai Pujiang Program 20PJ1415500, and the science research grants from the China Manned Space Project, grant No. CMS-CSST-2021-B06. K.T. was supported by JSPS KAKENHI (grant No. 20H05645).

Facility: Tianma 65 m (TMRT).

Software: GILDAS/CLASS (Guilloteau & Lucas 2000), astropy (Astropy Collaboration et al. 2013).

Appendix A
Line List of Molecular Lines

Table 3 shows the results of identification and Gaussian fitting of molecular lines, including RRLs that are blended with molecular lines. The unblended RRLs are listed in Table 4.

Table 3
Line List with Molecular Lines and Blended RRLs

f_{obs} (MHz)	Species	f_{rest} (MHz)	Transition J_{K_a,K_c}	E_u (K)	A_{ij} (10^{-6} s^{-1})	$\int T_{MB} dV$ (K km s^{-1})	ΔV (km s^{-1})	T_{MB}^{peak} (K)
34,824.24	C_2H_5CN	34,824.070	$4_{1,4} - 3_{1,3}$	5.3	3.04	0.94(5)	13(2)	7.04E−02
34,831.44	U					0.08(1)	3.7(9)	2.02E−02
34,857.29	^{34}SO	34,857.543	$N_J = 3_2 - 2_2$	20.9	0.2	1.71(5)	22(2)	7.20E−02
34,954.41	He89δ	34,954.331				0.48(5)	27(2)	1.66E−02
	HCN $v_2 = 1$	34,953.760	$12^- - 12^+$	1357.7	0.03			
35,135.15	H106η	35,132.748				2.68(2)	35.1(4)	7.19E−02
	H101ζ	35,135.235						
	CH_3OCH_3	35,135.469	$11_{5,6} - 12_{4,9}$	95.2	0.02			
	NH_3	35,134.303	(14,14)	1946.3	1.0			
35,161.34	$^{13}CH_3OH$	35,161.580	$7_{0,7} - 6_{1,6}$	63.4	0.2	0.49(7)	4.2(7)	1.09E−01

Note. (i) Doppler correction has been applied to f_{obs} assuming a source velocity of 6 km s^{-1} in LSR (Section 2.3). (ii) Rows with empty f_{obs} correspond to blended lines. (iii) Rows with a same species name, f_{rest}, and transition label correspond to different emission components of the same transition. (iv) The transition labels for HCN $v_t = 1$ are J^p where p is the parity. (v) The transition labels for CH_3OCH_3 are J_K^s where s is the symmetry substate. (vi) The transition labels are (J,K) for NH_3 convention lines. (vii) The transition labels for CH_3CN $v_t = 1$ are J_K^p where p is the parity. (viii) The numbers in brackets in Columns (7) and (8) represent the uncertainties of the last digits of the corresponding parameters.

(This table is available in its entirety in machine-readable form.)

Table 4
Line List with Unblended RRLs

f_{obs} (MHz)	Species	f_{rest} (MHz)	$\int T_{MB} dV$ (K km s^{-1})	ΔV (km s^{-1})	T_{MB}^{peak} (K)
34,941.26	H89δ	34,940.093	1.98(5)	19(2)	1.00E−01
35,150.59	He101ζ	35,149.553	0.10(1)	13(2)	7.41E−03
35,158.29	H81γ	35,157.272	5.44(7)	23.6(7)	2.17E−01
35,174.45	C81γ	35,174.814	0.05(1)	2.8(6)	1.67E−02
35,251.78	H71β	35,250.774	10.63(5)	24(2)	4.19E−01
35,266.15	He71β	35,265.138	0.84(1)	14.3(7)	5.52E−02
35,267.93	C71β	35,268.362	0.12(1)	5.1(7)	2.15E−02
35,457.42	H118κ	35,456.000	0.24(1)	14(1)	1.61E−02
35,522.92	H95ϵ	35,521.884	1.91(1)	24(2)	7.49E−02
35,598.08	H110θ	35,597.052	0.405(8)	17.4(7)	2.18E−02

Note. (i) Doppler correction has been applied to f_{obs} assuming a source velocity of 6 km s^{-1} in LSR (Section 2.3). (ii) Rows with empty f_{obs} correspond to blended lines. (iii) The numbers in brackets in Columns (4) and (5) represent the uncertainties of the last digits of the corresponding parameters.

(This table is available in its entirety in machine-readable form.)

Appendix B
Line List of RRLs Unblended with Molecular Lines

Table 4 shows the results of identification and Gaussian fitting of RRLs. The RRLs blended with molecular lines are not included (see Table 3).

ORCID iDs

Xunchuan Liu (刘训川) https://orcid.org/0000-0001-8315-4248
Tie Liu https://orcid.org/0000-0002-5286-2564
Zhiqiang Shen https://orcid.org/0000-0003-3540-8746
Qiuyi Luo https://orcid.org/0000-0003-4506-3171
Yu Cheng https://orcid.org/0000-0002-8691-4588
Qilao Gu https://orcid.org/0000-0002-2826-1902
Tianwei Zhang https://orcid.org/0000-0002-1466-3484
Sheng-Yuan Liu https://orcid.org/0000-0003-4603-7119
Xing Lu https://orcid.org/0000-0003-2619-9305
Juan Li https://orcid.org/0000-0003-3520-6191
Zhen Yan https://orcid.org/0000-0002-9322-9319
Chao Zhang https://orcid.org/0000-0002-5682-2906
Ken'ichi Tatematsu https://orcid.org/0000-0002-8149-8546
Hongli Liu https://orcid.org/0000-0003-3343-9645
Hsien Shang https://orcid.org/0000-0001-8385-9838
Fengwei Xu https://orcid.org/0000-0001-5950-1932
Chin-Fei Lee https://orcid.org/0000-0002-3024-5864
Chao Zhang https://orcid.org/0000-0002-5682-2906
Somnath Dutta https://orcid.org/0000-0002-2338-4583

References

Agúndez, M., Cernicharo, J., Quintana-Lacaci, G., et al. 2017, A&A, 601, A4
Astropy Collaboration, Robitaille, T. P., Tollerud, E. J., et al. 2013, A&A, 558, A33
Baldwin, J. A., Ferland, G. J., Martin, P. G., et al. 1991, ApJ, 374, 580
Bell, M. B., Avery, L. W., & Watson, J. K. G. 1993, ApJS, 86, 211
Belloche, A., Müller, H. S. P., Menten, K. M., Schilke, P., & Comito, C. 2013, A&A, 559, A47
Bernal, J. J., Koelemay, L. A., & Ziurys, L. M. 2021, ApJ, 906, 55
Boonman, A. M. S., van Dishoeck, E. F., Lahuis, F., et al. 2003, A&A, 399, 1047
Brocklehurst, M. 1971, MNRAS, 153, 471
Bruderer, S., Harsono, D., & van Dishoeck, E. F. 2015, A&A, 575, A94
Buhl, D., Snyder, L. E., Lovas, F. J., & Johnson, D. R. 1974, ApJL, 192, L97
Bussa, S. & VEGAS Development Team 2012, AAS Meeting, 219, 446.10
Cernicharo, J., Agúndez, M., Kaiser, R. I., et al. 2021, A&A, 652, L9
Chandler, C. J., & de Pree, C. G. 1995, ApJL, 455, L67
Combes, F., Gerin, M., Wootten, A., et al. 1987, A&A, 180, L13
Comito, C., Schilke, P., Phillips, T. G., et al. 2005, ApJS, 156, 127
Copetti, M. V. F., & Bica, E. L. D. 1983, Ap&SS, 91, 381
Cuadrado, S., Goicoechea, J. R., Pilleri, P., et al. 2015, A&A, 575, A82
Daly, A. M., Bermúdez, C., López, A., et al. 2013, ApJ, 768, 81
de Vicente, P., Martín-Pintado, J., Neri, R., & Colom, P. 2000, A&A, 361, 1058
Di Francesco, J., Johnstone, D., Kirk, H., MacKenzie, T., & Ledwosinska, E. 2008, ApJS, 175, 277
Dickens, J. E., Langer, W. D., & Velusamy, T. 2001, ApJ, 558, 693
Dicker, S. R., Mason, B. S., Korngut, P. M., et al. 2009, ApJ, 705, 226
Dong, J., Zhong, W., Wang, J., Liu, Q., & Shen, Z. 2018, ITAP, 66, 2044
Endres, C. P., Martin-Drumel, M.-A., Zingsheim, O., et al. 2021, JMoSp, 375, 111392
Esplugues, G. B., Cernicharo, J., Viti, S., et al. 2013a, A&A, 559, A51
Esplugues, G. B., Tercero, B., Cernicharo, J., et al. 2013b, A&A, 556, A143
Esplugues, G. B., Viti, S., Goicoechea, J. R., & Cernicharo, J. 2014, A&A, 567, A95
Feng, S., Beuther, H., Henning, T., et al. 2015, A&A, 581, A71
Friedel, D. N., & Widicus Weaver, S. L. 2012, ApJS, 201, 17
Genzel, R., & Stutzki, J. 1989, ARA&A, 27, 41
Goddi, C., Greenhill, L. J., Humphreys, E. M. L., et al. 2009, ApJ, 691, 1254
Gong, Y., Henkel, C., Thorwirth, S., et al. 2015, A&A, 581, A48
Gordon, M. A., & Sorochenko, R. L. 2002, Radio Recombination Lines. Their Physics and Astronomical Applications (Berlin: Springer)
Guilloteau, S., & Lucas, R. 2000, in ASP Conf. Ser. 217, Imaging at Radio through Submillimeter Wavelengths, ed. J. G. Mangum & S. J. E. Radford (San Francisco, CA: ASP), 299
Jacob, A. M., Menten, K. M., Gong, Y., et al. 2021, A&A, 647, A42
Johansson, L. E. B., Andersson, C., Ellder, J., et al. 1984, A&A, 130, 227
Jørgensen, J. K., Bourke, T. L., Nguyen Luong, Q., & Takakuwa, S. 2011, A&A, 534, A100
Kaifu, N., Ohishi, M., Kawaguchi, K., et al. 2004, PASJ, 56, 69
Lefloch, B., Ceccarelli, C., Codella, C., et al. 2017, MNRAS, 469, L73
Li, J., Shen, Z.-Q., Wang, J., et al. 2016, ApJ, 824, 136
Liu, S.-Y., Girart, J. M., Remijan, A., & Snyder, L. E. 2002, ApJ, 576, 255
Liu, T., Evans, N. J., Kim, K.-T., et al. 2020, MNRAS, 496, 2790
Liu, X., Wu, Y., Zhang, C., et al. 2022, A&A, 658, A140
Liu, X. C., Wu, Y., Zhang, C., et al. 2021, ApJ, 912, 148
Lloyd, S. 1982, ITIT, 28, 129
Luo, G., Feng, S., Li, D., et al. 2019, ApJ, 885, 82
Mangum, J. G., & Shirley, Y. L. 2015, PASP, 127, 266
Mangum, J. G., & Wootten, A. 1993, ApJS, 89, 123
McElroy, D., Walsh, C., Markwick, A. J., et al. 2013, A&A, 550, A36
McGuire, B. A., Burkhardt, A. M., Loomis, R. A., et al. 2020, ApJL, 900, L10
Mehringer, D. M., Pearson, J. C., Keene, J., & Phillips, T. G. 2004, ApJ, 608, 306
Menten, K. M., Reid, M. J., Forbrich, J., & Brunthaler, A. 2007, A&A, 474, 515
Menzel, D. H. 1968, Natur, 218, 756
Müller, H. S. P., Thorwirth, S., Roth, D. A., & Winnewisser, G. 2001, A&A, 370, L49
Natta, A., Walmsley, C. M., & Tielens, A. G. G. M. 1994, ApJ, 428, 209
Neill, J. L., Wang, S., Bergin, E. A., et al. 2013, ApJ, 770, 142
Olive, K. A., & Skillman, E. D. 2004, ApJ, 617, 29
Pardo, J. R., Cernicharo, J., Tercero, B., et al. 2022, A&A, 658, A39
Pickett, H. M., Poynter, R. L., Cohen, E. A., et al. 1998, JQSRT, 60, 883
Prozesky, A., & Smits, D. P. 2018, MNRAS, 478, 2766
Radford, H. E., & Kurtz, C. V. 1970, JRNBS, 74A, 791
Regemorter, H. V., & Prudhomme, M. 1979, JPhB, 12, 1053
Rizzo, J. R., Tercero, B., & Cernicharo, J. 2017, A&A, 605, A76
Rolffs, R., Schilke, P., Wyrowski, F., et al. 2011, A&A, 529, A76
Salgado, F., Morabito, L. K., Oonk, J. B. R., et al. 2017, ApJ, 837, 141
Schilke, P., Benford, D. J., Hunter, T. R., Lis, D. C., & Phillips, T. G. 2001, ApJS, 132, 281
Schilke, P., Groesbeck, T. D., Blake, G. A., & Phillips, T. G. 1997, ApJS, 108, 301
Shuping, R. Y., Morris, M., & Bally, J. 2004, AJ, 128, 363
Storey, P. J., & Hummer, D. G. 1995, MNRAS, 272, 41
Tahani, K., Plume, R., Bergin, E. A., et al. 2016, ApJ, 832, 12
Taniguchi, K., Saito, M., & Ozeki, H. 2016, ApJ, 830, 106
Tercero, B., Cernicharo, J., Pardo, J. R., & Goicoechea, J. R. 2010, A&A, 517, A96
Tercero, B., Vincent, L., Cernicharo, J., Viti, S., & Marcelino, N. 2011, A&A, 528, A26
Tercero, F., López-Pérez, J. A., Gallego, J. D., et al. 2021, A&A, 645, A37
Thaddeus, P., Mather, J., Davis, J. H., & Blair, G. N. 1974, ApJL, 192, L33
Turner, B. E. 1971, ApJL, 163, L35
Turner, B. E. 1989, ApJS, 70, 539
Turner, B. E., Zuckerman, B., Palmer, P., & Morris, M. 1973, ApJ, 186, 123
Wang, J. Q., Yu, L. F., Jiang, Y. B., et al. 2017, AcASn, 58, 37
Wang, S., Bergin, E. A., Crockett, N. R., et al. 2011, A&A, 527, A95
White, G. J., Araki, M., Greaves, J. S., Ohishi, M., & Higginbottom, N. S. 2003, A&A, 407, 589
Wilson, T. L., Filges, L., Codella, C., Reich, W., & Reich, P. 1997, A&A, 327, 1177
Wilson, T. L., Henkel, C., Huttemeister, S., et al. 1993, A&A, 276, L29
Wilson, T. L., & Rood, R. 1994, ARA&A, 32, 191
Wu, Y., Lin, L., Liu, X., et al. 2019a, A&A, 627, A162
Wu, Y., Liu, T., & Qin, S.-L. 2014, ApJ, 791, 123
Wu, Y., Liu, X., Chen, X., et al. 2019b, MNRAS, 488, 495
Xie, J., Fuller, G. A., Li, D., et al. 2021, SCPMA, 64, 279511
Zhang, X.-Y., Zhu, Q.-F., Li, J., et al. 2017, A&A, 606, A74
Zhong, W.-Y., Dong, J., Gou, W., et al. 2018, RAA, 18, 044
Zhu, F.-Y., Wang, J., Zhu, Q.-F., & Zhang, J.-S. 2022, A&A, 665, A94
Zhu, F.-Y., Zhu, Q.-F., Wang, J.-Z., & Zhang, J.-S. 2019, ApJ, 881, 14
Zou, L., & Widicus Weaver, S. L. 2017, ApJ, 849, 139
Zuckerman, B., Palmer, P., Penfield, H., & Lilley, A. E. 1967, ApJL, 149, L61